Eur. Phys. J. E (2018) **41**: 17
DOI 10.1140/epje/i2018-11622-y

THE EUROPEAN PHYSICAL JOURNAL E

Regular Article

An alternative method to implement contact angle boundary condition and its application in hybrid lattice-Boltzmann finite-difference simulations of two-phase flows with immersed surfaces

Jun-Jie Huang[1,2,3,a], Jie Wu[4], and Haibo Huang[5]

[1] Department of Engineering Mechanics, College of Aerospace Engineering, Chongqing University, Chongqing 400044, China
[2] Chongqing Key Laboratory of Heterogeneous Material Mechanics (Chongqing University), Chongqing 400044, China
[3] State Key Laboratory of Mechanical Transmission, Chongqing University, Chongqing 400044, China
[4] Department of Aerodynamics, Nanjing University of Aeronautics and Astronautics, Yudao Street 29, Nanjing, Jiangsu 210016, China
[5] Department of Modern Mechanics, University of Science and Technology of China, Hefei, Anhui 230026, China

Received 12 September 2017 and Received in final form 26 November 2017
Published online: 7 February 2018 – © EDP Sciences / Società Italiana di Fisica / Springer-Verlag 2018

Abstract. We propose an alternative method to implement the contact angle boundary condition on a solid wall and apply it in hybrid lattice-Boltzmann finite-difference simulations of two-phase flows with immersed surfaces in which the flow equations are solved by the lattice-Boltzmann method and the interface equations are solved by the finite-difference method. Using the hyperbolic tangent profile of the order parameter across an interface in phase-field theory, we were able to obtain its unknown value at a ghost point from the information at only one point in the fluid domain. This is in contrast with existing approaches relying on interpolations involving several points. The special feature allows it to be more easily implemented on immersed surfaces cutting through the grid lines. It was properly incorporated into the framework of the hybrid lattice-Boltzmann finite-difference simulation, and applied successfully for several problems with different levels of complexity. First, the equilibrium shapes of a droplet on a sphere with different contact angles and radii were studied under cylindrical geometry and a good agreement with theoretical predictions was found. Preliminary studies on a three-dimensional droplet spreading on a sphere were also performed and the results agreed well with the corresponding axisymmetric results. Second, the spreading of a two-dimensional drop on an embedded inclined wall with a given contact angle was investigated and the results matched those on a flat wall at the domain boundary under the same condition. Third, capillary filling in a cylindrical tube was studied and the speed of the interface in the tube was found to follow Washburn's law. Fourth, a droplet impacting on a sphere was investigated and several different outcomes were captured depending on the Reynolds number, the viscosity ratio, and the wettability and radius of the sphere. Finally, the proposed method was shown to be capable of studying even more complicated problems involving the interaction between a droplet and multiple objects of different sizes and contact angles.

1 Introduction

Two-phase flows with moving contact lines (MCLs) are commonly encountered in various areas of our daily life and a number of industries [1]. Numerical simulations of such flows have recently had significant development [2]. Fluid flows with interfaces are often simulated by either the interface tracking approach or the interface capturing approach. The volume-of-fluid (VOF) method [3], level-set method (LSM) [4] and phase-field or diffuse-interface method (DIM) [5], all belonging to the latter category, are probably the most commonly used. So far, numerical work mostly focused on two-phase flows in the bulk region or near flat substrates while those over curved surfaces are less studied due to the difficulty to handle the complex boundary. In the DIM, a physically defined indicator function, known as the order parameter (or the concentration), is used to differentiate the two fluids. The evolution of the order parameter is usually described by the Cahn-Hilliard equation (CHE) [6, 7]. An important component in phase-field–based simulations is the wetting boundary condition (WBC) on a solid surface with specified wettability characterized by a contact angle. There are several formulations for the WBC and some comparative studies

[a] e-mail: jjhuang@cqu.edu.cn (corresponding author)

have been performed in [8]. Among various WBCs, the geometric formulation has the property to always keep the local contact angle at the specified value [9, 10]. As far as we know, most of the previous studies using the geometric formulation on a Cartesian mesh dealt with a flat surface as the boundary of the simulation domain. How to implement it on solid surfaces of general shapes immersed inside the domain has been rarely investigated. One exception is the recent work by Liu and Ding [11] who extended the characteristic interpolation (CI) originally proposed by Lee and Kim [10] to curved surfaces. When the CI is used to implement the WBC on general surfaces, one has to determine the local configuration of the interface before applying any interpolation formula to obtain the unknown value (of the order parameter) along the characteristic line [11]. This is mainly because at different places an immersed curved surface has different orientations and intersects the Cartesian mesh in different ways. Thus, the implementation of the WBC using the original CI is relatively complex and it becomes even more involved if the immersed surface moves (in that case one has to determine the local configuration at each time step). Quite recently another method was proposed by Fakhari and Bolster [12] to implement the WBC on curved boundaries where the surface energy formulation was adopted. Despite that some approximations based on certain assumptions were made, their method still involves complicated interpolations [12]. One of the main purposes of the present work is to propose an alternative method to implement the WBC on general immersed surfaces that does not rely on complex interpolations. The fundamental idea is to find the unknown order parameter along the direction normal to the interface (instead of that parallel to the interface as in previous works) by making full use of its hyperbolic tangent profile across the interface (as illustrated below).

In the literature there are limited works on two-phase flows over curved surfaces, and three-dimensional (3-D) or axisymmetric simulations are even fewer because of the increased complexity. Ge and Fan [13] combined the level-set method (LSM) and the immersed-boundary method (IBM) to simulate the collision between a 3-D evaporative droplet and a spherical particle at high temperature and obtained good agreement with corresponding experiments. Because the particle is very hot, a vapor layer exists between the droplet and the particle surface, and wetting was not included in [13] (instead, a vapor-layer model was employed). Li and Wang [14] also used the LSM and IBM to study a 3-D droplet impacting on a sphere at low speed. Unlike [13], their simulations were under the isothermal condition and the droplet had wetting contact with the sphere. A static contact angle model was included within the framework of the LSM in [14]. Zhang *et al.* [15] employed the Shan-Chen multiphase lattice-Boltzmann method (LBM) to study a 3-D droplet impinging on flat and spherical surfaces. They investigated the morphology of the droplet during the impact process and focused on the variation of the film thickness at the north pole of the sphere. The single-relaxation-time collision model was adopted and the Reynolds and Weber numbers were relatively low in [15]. Liu and Ding [11] combined the DIM and IBM to perform axisymmetric simulations of water entry of a sphere and also of a drop impacting on a sphere. They successfully captured the complicated water entry process and obtained a good agreement with experiments. Liu *et al.* [16] employed the phase-field LBM (in which the interface equations are based on the phase-field theory and the flow and interface equations are solved by LBM) to study a 3-D drop impacting on an asymmetric curved surface and verified the symmetry breaking in drop bouncing observed in their experiments. It is noted that the curved surface was modelled as a series of steps and the surface representation is not very precise in [16]. It appears that 3-D or axisymmetric studies of multiphase flows over curved surfaces are still quite scarce in the literature. Among them, axisymmetric simulations are even rarer. For many 3-D problems with sufficient symmetry, it is much more economic to employ the axisymmetric approach than the full 3-D one. As of now, we are not aware of any work that employs LBM to do such axisymmetric studies over curved surfaces. It is known that on a Cartesian mesh LBM is advantageous to deal with complex geometries as compared with other methods directly solving the Navier-Stokes equations (NSEs). Thus, another purpose of this paper is to employ a LBM-based hybrid method using the newly proposed WBC to simulate axisymmetric two-phase flows over immersed curved surfaces.

The remainder of this work is organized as follows. Section 2 introduces the theoretical and numerical methodology with the emphasis on the newly proposed method. Section 3 presents the studies of several two-dimensional (2-D), axisymmetric and 3-D problems to verify it within the framework of hybrid lattice-Boltzmann finite-difference simulation and to show its capability to capture complex fluid interface evolutions when immersed curved surfaces are present. Section 4 concludes this paper.

2 Theoretical and numerical methodology

The present simulations of two immiscible fluids use a hybrid lattice-Boltzmann finite-difference approach [17]. The Cahn-Hilliard equation (CHE) for the interface dynamics based on phase-field theory is solved by a finite-difference method. The hydrodynamics of the flow is simulated by the LBM (the current versions of LBM are mainly based on [17–19]). For completeness, some key components are briefly recaptured below first. The newly proposed WBC will be described in detail.

2.1 Phase-field model for interface dynamics

For a system of binary fluids, a free energy functional $\mathcal{F}$ may be defined as

$$\mathcal{F}(\phi, \boldsymbol{\nabla}\phi) = \int_V \left(\Psi(\phi) + \frac{1}{2}\kappa |\boldsymbol{\nabla}\phi|^2 \right) \mathrm{d}V, \qquad (1)$$

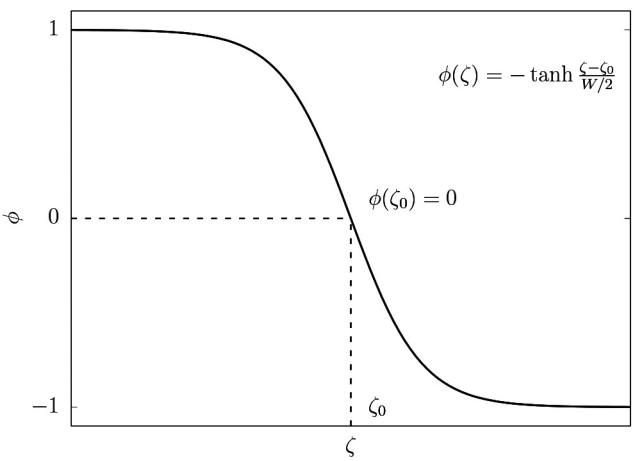

Fig. 1. The hyperbolic tangent profile of the order parameter across a flat interface in equilibrium.

where $\Psi(\phi)$ is the bulk free energy density, and the second term is the interfacial energy density (κ is a constant). With $\Psi(\phi)$ chosen to be in the double-well form, $\Psi(\phi) = a(\phi^2-1)^2$ (a is a constant), the order parameter ϕ varies between 1 in one of the fluids (labelled as *liquid* for convenience) and -1 in the other (labelled as *gas*). The chemical potential μ is obtained by taking the variation of $\mathcal{F}$ with respect to ϕ,

$$\mu = \frac{\delta\mathcal{F}}{\delta\phi} = \frac{\mathrm{d}\Psi(\phi)}{\mathrm{d}\phi} - \kappa\nabla^2\phi = 4a\phi(\phi^2-1) - \kappa\nabla^2\phi. \quad (2)$$

The coefficients a and κ are related to the interfacial tension σ and interface thickness W as $a = \frac{3\sigma}{4W}$ and $\kappa = \frac{3\sigma W}{8}$ [20]. Across a flat interface in equilibrium ϕ follows a hyperbolic tangent profile $\phi(\zeta) = -\tanh\frac{\zeta-\zeta_0}{W/2}$ where ζ is the coordinate along the axis normal to the interface, and ζ_0 is the position where $\phi = 0$ (see fig. 1). With contribution due to convection taken into account, the CHE reads [6],

$$\frac{\partial\phi}{\partial t} + \boldsymbol{u}\cdot\boldsymbol{\nabla}\phi = \boldsymbol{\nabla}\cdot(M\boldsymbol{\nabla}\mu), \quad (3)$$

where M is the (constant) mobility, and $\boldsymbol{u}$ is the local fluid velocity.

Equations (2) and (3) are discretized in space by the 2nd-order finite-difference method and integrated in time by the 4th-order Runge-Kutta method. In this work we use a uniform grid size δ_x and time step δ_t. The 1st- and 2nd-order spatial derivatives are obtained by the 2nd-order isotropic scheme based on the D2Q9 and D3Q19 velocity model in LBM in two and three dimensions, respectively. Taking the order parameter ϕ in 2-D as an example, we use

$$\frac{\partial\phi}{\partial x} = \frac{3}{c\delta_x}\sum_{i=1}^{8} w_i e_{ix}\phi(\boldsymbol{x}+\boldsymbol{e}_i\delta_t), \quad (4)$$

$$\frac{\partial\phi}{\partial y} = \frac{3}{c\delta_x}\sum_{i=1}^{8} w_i e_{iy}\phi(\boldsymbol{x}+\boldsymbol{e}_i\delta_t), \quad (5)$$

$$\frac{\partial^2\phi}{\partial x^2} + \frac{\partial^2\phi}{\partial y^2} = \frac{6}{\delta_x^2}\left[\sum_{i=1}^{8} w_i\phi(\boldsymbol{x}+\boldsymbol{e}_i\delta_t) - (1-w_0)\phi(\boldsymbol{x})\right], \quad (6)$$

where $c = \delta_x/\delta_t$ is the lattice velocity (magnitude). The lattice velocity (vector) $\boldsymbol{e}_i$ for D2Q9 is given by

$$\boldsymbol{e}_i = (e_{ix}, e_{iy}) = \begin{cases} (0,0), & \text{for } i=0, \\ \left(\cos\left[\frac{(i-1)\pi}{2}\right], \sin\left[\frac{(i-1)\pi}{2}\right]\right)c, & \text{for } i=1,2,3,4, \\ \left(\cos\left[\frac{(2i-9)\pi}{4}\right], \sin\left[\frac{(2i-9)\pi}{4}\right]\right)c, & \text{for } i=5,6,7,8, \end{cases} \quad (7)$$

and w_i is the weight associated with the i-th direction,

$$w_i = \begin{cases} \frac{4}{9}, & \text{for } i=0, \\ \frac{1}{9}, & \text{for } i=1,2,3,4, \\ \frac{1}{36}, & \text{for } i=5,6,7,8. \end{cases} \quad (8)$$

Suitable boundary conditions are required by eqs. (2) and (3). For the chemical potential μ, we employ the no-flux condition on a surface S,

$$\boldsymbol{n}_S\cdot\boldsymbol{\nabla}\mu|_S = \left.\frac{\partial\mu}{\partial n_S}\right|_S = 0, \quad (9)$$

where $\boldsymbol{n}_S$ denotes the unit normal vector on S pointing *into* the fluid. The boundary condition for ϕ basically follows the geometric formulation [9,10]. It is assumed that the contours of ϕ in the diffuse interface are parallel to each other everywhere. Besides, we also assume that in the direction normal to the interface, the hyperbolic tangent profile of ϕ is well preserved (or just slightly perturbed). The direct use of this profile makes the current method distinct from previous works (*e.g.*, [9–11]). Figure 2 illustrates the implementation of the boundary condition for ϕ on an arbitrarily positioned wall with a specified contact angle θ_w immersed in the fluid domain in 2-D. We consider a point (x_0, y_0) on the grid in the fluid near the wall. When the grid is fine enough to resolve the largest curvature of the wall, it is reasonable to assume that locally the wall can be approximated by a straight line. The eight points surrounding (x_0, y_0) on the grid may be divided into two groups: those on the same side of the line as (x_0, y_0) (Group-S) and those on the other side of the line (Group-O). The WBC is used to obtain the values of ϕ at the ghost points belonging to Group-O, which are required to calculate the derivatives $\frac{\partial\phi}{\partial x}$, $\frac{\partial\phi}{\partial y}$ and $\nabla^2\phi$ at (x_0, y_0). We take one of the ghost points, (x_v, y_v) in fig. 2 as an example. The specific steps to obtain $\phi(x_v, y_v)$ are described below. For convenience, a vector $\boldsymbol{n} = \cos\theta\boldsymbol{e}_x + \sin\theta\boldsymbol{e}_y$ ($\boldsymbol{e}_x$ and $\boldsymbol{e}_y$ are the unit vectors in x- and y-directions) in the x-y plane is sometimes represented by a complex variable $e^{i\theta} = \cos\theta + i\sin\theta$.

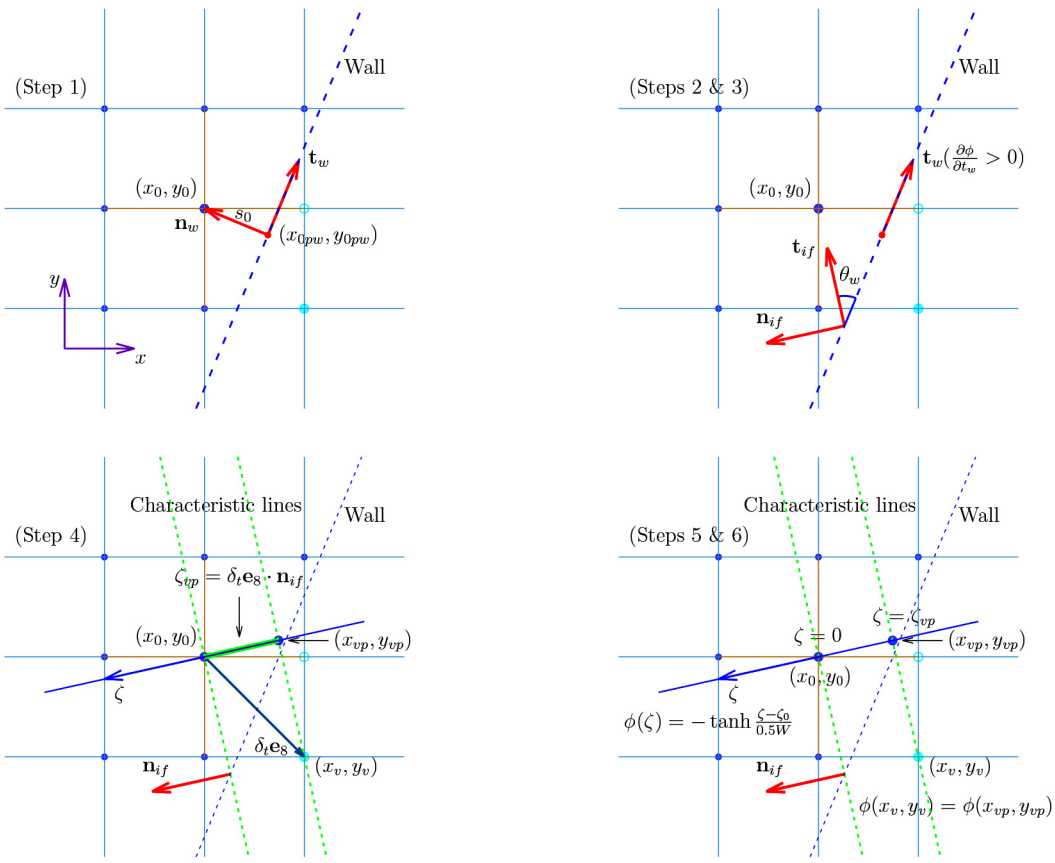

Fig. 2. Illustration of the proposed implementation of the wetting boundary condition for the order parameter ϕ on an immersed wall with a contact angle θ_w.

- Step 1: To determine the local directions that are normal and tangential to the wall, $\boldsymbol{n}_w$ and $\boldsymbol{t}_w = \boldsymbol{n}_w e^{i(-\frac{\pi}{2})}$, where $\boldsymbol{n}_w = (x_0 - x_{0pw}, y_0 - y_{0pw})/s_0$, the point (x_{0pw}, y_{0pw}) is the projection of (x_0, y_0) onto the wall, and s_0 is the distance between (x_{0pw}, y_{0pw}) and (x_0, y_0).
- Step 2: To determine the sign of the local tangential gradient of ϕ, $\frac{\partial\phi}{\partial t_w}$, using the values of ϕ at (some of) the points in Group-S, so as to determine the direction of the characteristic lines parallel to the interface: $\boldsymbol{t}_{if} = \boldsymbol{t}_w e^{i\theta_w}$ if $\frac{\partial\phi}{\partial t_w} > 0$ (as in fig. 2) and $\boldsymbol{t}_{if} = \boldsymbol{t}_w e^{i(\pi-\theta_w)}$ if $\frac{\partial\phi}{\partial t_w} < 0$ (another situation not shown here).
- Step 3: To calculate the direction normal to the characteristic lines $\boldsymbol{n}_{if} = \boldsymbol{t}_{if} e^{i\frac{\pi}{2}}$ (note the gradient of ϕ along $\boldsymbol{n}_{if}$ is ensured to be negative, *i.e.*, $\frac{\partial\phi}{\partial n_{if}} < 0$).
- Step 4: To project the point (x_v, y_v) to the line passing through (x_0, y_0) along the direction $\boldsymbol{n}_{if}$ to obtain the point (x_{vp}, y_{vp}), and to further calculate its coordinate on the ζ-axis in fig. 2 (denoted as ζ_{vp}). Note that the projection of (x_0, y_0) to the ζ-axis is the point itself and we set $\zeta = 0$ at (x_0, y_0). Suppose $(x_v, y_v) = (x_0 + e_{m,x}\delta_t, y_0 + e_{m,y}\delta_t)$ ($\boldsymbol{e}_m$ is the lattice velocity along the m-th direction, $m = 8$ in fig. 2), ζ_{vp} can be simply calculated as $\zeta_{vp} = \delta_t \boldsymbol{e}_m \cdot \boldsymbol{n}_{if}$ without computing (x_{vp}, y_{vp}).
- Step 5: To calculate the parameter ζ_0 which gives $\phi(\zeta_0) = 0$ so that the hyperbolic tangent profile of ϕ along the ζ-axis, $\phi(\zeta) = -\tanh\frac{\zeta-\zeta_0}{W/2}$, is fully determined. Note that Newton's method is employed to solve the nonlinear equation $\phi|_{\zeta=0} = -\tanh(-2\zeta_0/W) = \phi(x_0, y_0)$ to find ζ_0.
- Step 6: To calculate the order parameter ϕ at (x_{vp}, y_{vp}) as $\phi(x_{vp}, y_{vp}) = \phi(\zeta_{vp}) = -\tanh\frac{\zeta_{vp}-\zeta_0}{W/2}$. The value of ϕ at (x_v, y_v) is obtained as $\phi(x_v, y_v) = \phi(x_{vp}, y_{vp})$ because the two points are on the same characteristic line.

It is obvious that the above steps involve at most nine points (including (x_0, y_0) and its eight neighbours). The neighbouring points in Group-S are actually just used to roughly determine the interface orientation. In essence, the unique feature of the present method is due to Steps 4 and 5. By *projecting the ghost point onto the ζ-axis and employing the hyperbolic tangent profile of ϕ in this direction*, we circumvent the usual interpolation step to find $\phi(x_v, y_v)$ in previous methods which may become quite complex as it involves the determination of the local interface configuration in the grid lines [11]. One might worry that the solution of the nonlinear equation brings additional cost. According to our experience, the convergence in the solution process to find ζ_0 by Newton's method

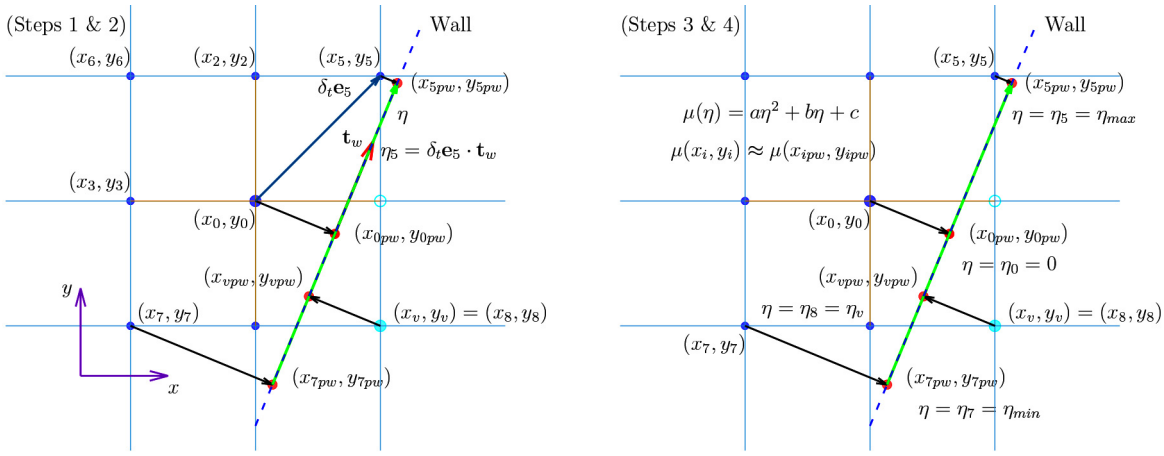

Fig. 3. Illustration of the proposed implementation of the boundary condition for the chemical potential μ on an immersed wall.

is quite fast. What is more, the above WBC is applied only in the interfacial region (set according to the criterion $|\phi(x_0, y_0)| < 0.99$) which just covers a few grid points. When $\phi(x_0, y_0) > 0.99$, the value of ϕ at the ghost point $\phi(x_v, y_v)$ is simply set to be 1, and when $\phi(x_0, y_0) < -0.99$, it is set to be -1. Therefore, the additional computational cost is quite small. For the chemical potential μ, the no-flux condition on a wall is applied and its implementation is illustrated in fig. 3. There are some differences between this implementation for μ and the above for ϕ since the chemical potential does not obey the hyperbolic tangent profile and the condition for μ is independent of the contact angle θ_w. The implementation for μ involves more points surrounding (x_0, y_0) (but still limited to the nearest and next-to-nearest neighbours). For convenience, the eight neighbours are labelled with the index i ($i = 1, 2, \cdots, 8$) corresponding to the D2Q9 velocity model (for clarity, (x_1, y_1) and (x_4, y_4) are not labelled in fig. 3). The specific steps to obtain $\mu(x_v, y_v)$ are as follows.

- Step 1: To project all nine points (x_i, y_i) ($i = 0, 1, \cdots, 8$) onto the wall to obtain nine points on the wall (x_{ipw}, y_{ipw}) ($i = 0, 1, \cdots, 8$) and calculate their coordinates on the η-axis (along the wall) as $\eta_i = \delta_t \boldsymbol{e}_i \cdot \boldsymbol{t}_w$ (without actually knowing (x_{ipw}, y_{ipw})). Note that $\eta_0 = 0$ is at (x_{0pw}, y_{0pw}).
- Step 2: Among the neighbouring points in Group-S search for the two indices with the maximum and minimum η, denoted as $i_{\max}$ and $i_{\min}$ (for example, $i_{\max} = 5$ and $i_{\min} = 7$ in fig. 3).
- Step 3: Upon assuming a quadratic polynomial for the variation of μ along the η-axis, $\mu = a\eta^2 + b\eta + c$, to solve for the coefficients a, b, and c from the three known conditions $\mu(0) = \mu(x_{0pw}, y_{0pw}) \approx \mu(x_0, y_0)$, $\mu(\eta_{i_{\max}}) = \mu(x_{i_{\max}pw}, y_{i_{\max}pw}) \approx \mu(x_{i_{\max}}, y_{i_{\max}})$, and $\mu(\eta_{i_{\min}}) = \mu(x_{i_{\min}pw}, y_{i_{\min}pw}) \approx \mu(x_{i_{\min}}, y_{i_{\min}})$.
- Step 4: The value of μ at (x_{vpw}, y_{vpw}) is found by substituting the coordinate η_v into the polynomial, $\mu(\eta_v) = a\eta_v^2 + b\eta_v + c$. The value of μ at (x_v, y_v) is also obtained as $\mu(x_v, y_v) \approx \mu(x_{vpw}, y_{vpw})$.

It is noted that one can prove that the above approximation $\mu(x_{ipw}, y_{ipw}) \approx \mu(x_i, y_i)$ is 2nd-order accurate using the no-flux condition eq. (9) on the wall.

The above method can be extended to 3-D. In 3-D, we consider a point (x_0, y_0, z_0) on the grid in the fluid near the wall and use the D3Q19 velocity model [21]. It is reasonable to assume that locally the wall can be approximated by a plane when the grid is fine enough. The eighteen points surrounding (x_0, y_0, z_0) (related to the D3Q19 model) may be divided into two groups (Group-S and Group-O) depending on whether the neighbour is on the same side of the plane as (x_0, y_0, z_0). The aim is to obtain the values of ϕ at the ghost points belonging to Group-O. Suppose the unit normal vector of the local plane within the interface is $\boldsymbol{n}_w = n_{w,x}\boldsymbol{e}_x + n_{w,y}\boldsymbol{e}_y + n_{w,z}\boldsymbol{e}_z$. The spatial gradient of ϕ can be expressed as

$$\boldsymbol{\nabla}\phi = \frac{\partial \phi}{\partial x}\boldsymbol{e}_x + \frac{\partial \phi}{\partial y}\boldsymbol{e}_y + \frac{\partial \phi}{\partial z}\boldsymbol{e}_z = \frac{\partial \phi}{\partial n_w}\boldsymbol{n}_w + \frac{\partial \phi}{\partial t_w}\boldsymbol{t}_w. \quad (10)$$

Within the local plane the gradient of ϕ is along the direction $\boldsymbol{t}_w$ (for convenience, we select the unit vector $\boldsymbol{t}_w$ that satisfies $\frac{\partial \phi}{\partial t_w} > 0$). Unlike in 2-D, $\boldsymbol{t}_w$ has to be determined first in 3-D. The following steps are employed to find $\boldsymbol{t}_w$. First, the values of $\frac{\partial \phi}{\partial x}$, $\frac{\partial \phi}{\partial y}$ and $\frac{\partial \phi}{\partial z}$ are approximated by finite-difference schemes using the points in Group-S. Then $\frac{\partial \phi}{\partial n_w}$ and $\frac{\partial \phi}{\partial t_w}$ are computed as

$$\frac{\partial \phi}{\partial n_w} = \boldsymbol{n}_w \cdot \boldsymbol{\nabla}\phi = n_{w,x}\frac{\partial \phi}{\partial x} + n_{w,y}\frac{\partial \phi}{\partial y} + n_{w,z}\frac{\partial \phi}{\partial z}, \quad (11)$$

$$\frac{\partial \phi}{\partial t_w} = \sqrt{\left(\frac{\partial \phi}{\partial x}\right)^2 + \left(\frac{\partial \phi}{\partial y}\right)^2 + \left(\frac{\partial \phi}{\partial z}\right)^2 - \left(\frac{\partial \phi}{\partial n_w}\right)^2}. \quad (12)$$

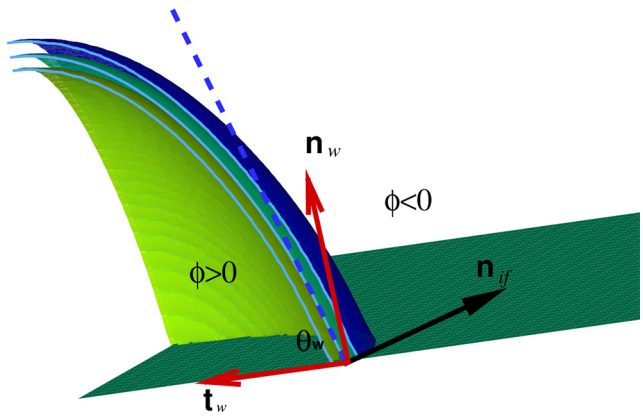

Fig. 4. Illustration for the implementation in 3-D.

By projecting eq. (10) in x-, y- and z-directions, we find the vector $\boldsymbol{t}_w = t_{w,x}\boldsymbol{e}_x + t_{w,y}\boldsymbol{e}_y + t_{w,z}\boldsymbol{e}_z$ as

$$\begin{aligned} t_{w,x} &= \frac{1}{\partial\phi/\partial t_w}\left(\frac{\partial\phi}{\partial x} - \frac{\partial\phi}{\partial n_w}n_{w,x}\right), \\ t_{w,y} &= \frac{1}{\partial\phi/\partial t_w}\left(\frac{\partial\phi}{\partial y} - \frac{\partial\phi}{\partial n_w}n_{w,y}\right), \\ t_{w,z} &= \frac{1}{\partial\phi/\partial t_w}\left(\frac{\partial\phi}{\partial z} - \frac{\partial\phi}{\partial n_w}n_{w,z}\right). \end{aligned} \tag{13}$$

With $\boldsymbol{n}_w$, $\boldsymbol{t}_w$ and the contact angle θ_w, the unit vector normal to the interface $\boldsymbol{n}_{if}$ ($\frac{\partial\phi}{\partial n_{if}} < 0$) is found as (see fig. 4),

$$\boldsymbol{n}_{if} = \cos\theta_w \boldsymbol{n}_w + (-\sin\theta_w)\boldsymbol{t}_w. \tag{14}$$

Now the problem is transformed from 3-D into 2-D (inside the plane determined by $\boldsymbol{n}_w$ and $\boldsymbol{t}_w$). Subsequent steps are similar to the above for 2-D. It is noted that the extension of the above steps in 2-D to find the unknown chemical potential to 3-D is not straightforward. After projecting the points onto the wall (*i.e.*, the local plane), more complex searching and interpolations have to be performed in the plane if one follows the steps in 2-D. In the present work, we use a simplified implementation for 3-D problems (which does not seem to incur unacceptable errors). For a point $(x_v, y_v, z_v) = (x_0 + e_{m,x}\delta_t, y_0 + e_{m,y}\delta_t, z_0 + e_{m,z}\delta_t)$ in Group-O, we simply set $\mu(x_v, y_v, z_v) \approx \mu(x_0, y_0, z_0)$. This approximation can be only 1st-order accurate in the worst case and 2nd-order accurate in the best case, depending on the two vectors $\boldsymbol{n}_w$ and $\boldsymbol{e}_m$ $(= e_{m,x}\boldsymbol{e}_x + e_{m,y}\boldsymbol{e}_y + e_{m,z}\boldsymbol{e}_z)$: 2nd-order accuracy is achieved when $|\boldsymbol{n}_w \cdot \boldsymbol{e}_m|/|\boldsymbol{e}_m| = 1$ (*i.e.*, $\boldsymbol{n}_w$ and $\boldsymbol{e}_m$ are parallel to each other) whereas the accuracy is degraded if $|\boldsymbol{n}_w \cdot \boldsymbol{e}_m|/|\boldsymbol{e}_m| < 1$.

2.2 Lattice-Boltzmann method for hydrodynamics

The present work deals with 2-D, 3-D and axisymmetric problems. The lattice-Boltzmann model for axisymmetric problems differs in many aspects from the other two. The D2Q9 velocity model is adopted for both the 2-D and axisymmetric models whereas the D3Q19 velocity model is used for the 3-D model. First, the 2-D LBM is briefly introduced. When the single-relaxation-time collision model is used, the lattice-Boltzmann equations (LBEs) read [18],

$$\begin{aligned} &f_i(\boldsymbol{x} + \boldsymbol{e}_i\delta_t, t + \delta_t) - f_i(\boldsymbol{x}, t) = \\ &-\frac{1}{\tau_f}(f_i - f_i^{eq}) + \left(1 - \frac{1}{2\tau_f}\right)(\boldsymbol{e}_i - \boldsymbol{u}) \\ &\cdot[\boldsymbol{\nabla}\rho c_s^2(\Gamma_i - \Gamma_i(0)) - \phi\boldsymbol{\nabla}\mu\Gamma_i], \end{aligned} \tag{15}$$

where f_i and f_i^{eq} are the distribution functions (DFs) and equilibrium DFs along the direction of the lattice velocity $\boldsymbol{e}_i$ $(i = 0, 1, \cdots, b)$, w_i is the weight for the direction along $\boldsymbol{e}_i$, c_s is the lattice sound speed ($c = \sqrt{3}c_s$ for D2Q9), τ_f is the relaxation parameter, and δ_t is the time step. The density ρ is computed from the order parameter ϕ as

$$\rho(\phi) = \frac{\phi + 1}{2}\rho_L + \frac{1 - \phi}{2}\rho_G, \tag{16}$$

where ρ_L and ρ_G denote the densities of the liquid and gas. The dynamic viscosities of the liquid as gas are $\eta_L = \rho_L\nu_L$ and $\eta_G = \rho_G\nu_G$, where ν_L and ν_G are their kinematic viscosities. The kinematic viscosity ν is computed from the order parameter ϕ as [19],

$$\frac{1}{\nu(\phi)} = \frac{\phi + 1}{2}\frac{1}{\nu_L} + \frac{1 - \phi}{2}\frac{1}{\nu_G}. \tag{17}$$

The relaxation parameter τ_f is related to the kinematic viscosity as $\nu = c_s^2(\tau_f - 0.5)\delta_t$. The equilibrium DFs are given by

$$f_i^{eq} = w_i\left[p + \rho c_s^2\left(\frac{1}{c_s^2}e_{i\alpha}u_\alpha + \frac{1}{2c_s^4}(e_{i\alpha}e_{i\beta} - c_s^2\delta_{\alpha\beta})u_\alpha u_\beta\right)\right], \tag{18}$$

where p is the hydrodynamic pressure, and the term Γ_i in eq. (15) is given by

$$\Gamma_i(\boldsymbol{u}) = w_i\left[1 + \frac{1}{c_s^2}e_{i\alpha}u_\alpha + \frac{1}{2c_s^4}(e_{i\alpha}e_{i\beta} - c_s^2\delta_{\alpha\beta})u_\alpha u_\beta\right]. \tag{19}$$

The macroscopic variables are calculated as

$$p = \sum_i f_i + \frac{1}{2}\delta_t(\boldsymbol{u}\cdot\boldsymbol{\nabla}\rho c_s^2), \tag{20}$$

$$\rho\boldsymbol{u} = \frac{1}{c_s^2}\sum_i f_i\boldsymbol{e}_i - \frac{1}{2}\delta_t(\phi\boldsymbol{\nabla}\mu). \tag{21}$$

Through the Chapman-Enskog analysis, it can be found that the LBEs, eq. (15), approximate the following equations at the macroscopic level [19]:

$$\frac{\partial p}{\partial t} + \rho c_s^2\boldsymbol{\nabla}\cdot\boldsymbol{u} = 0, \tag{22}$$

$$\rho\left(\frac{\partial\boldsymbol{u}}{\partial t} + \boldsymbol{u}\cdot\boldsymbol{\nabla}\boldsymbol{u}\right) = -\boldsymbol{\nabla}p - \phi\boldsymbol{\nabla}\mu + \boldsymbol{\nabla}\cdot\boldsymbol{\Pi}, \tag{23}$$

where $\boldsymbol{\Pi}$ is the common viscous stress tensor for Newtonian fluids and the term $-\phi\boldsymbol{\nabla}\mu$ represents the effect of

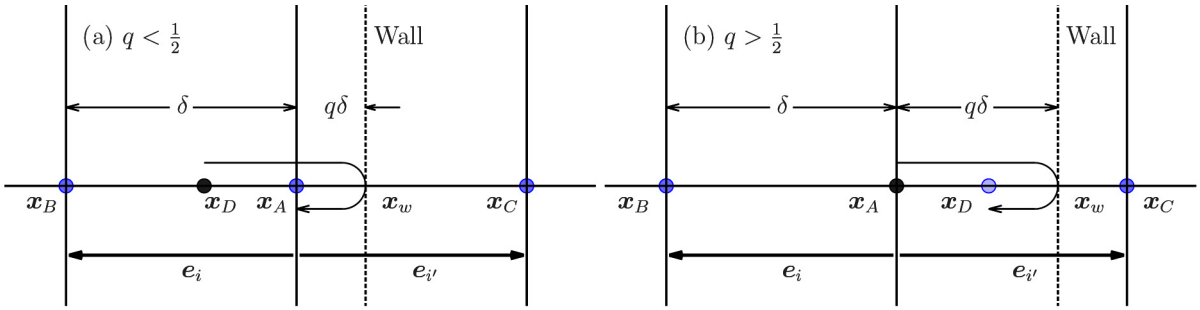

Fig. 5. The interpolated bounce-back method to obtain the unknown distribution function at a site near the wall (spatial linear interpolation is used). Note δ is the distance between two neighbouring points along a given direction $\boldsymbol{e}_i$: $\delta = \delta_x$ for $i = 1, 2, 3, 4$ and $\delta = \sqrt{2}\delta_x$ for $i = 5, 6, 7, 8$ when the D2Q9 velocity model is adopted.

the interfacial tension force. To improve stability, we actually used the multiple-relaxation-time (MRT) collision model [22]. The basic formulation of the 3-D LBM is almost the same as the 2-D LBM except that the MRT collision model for D3Q19 [21] is used and the interfacial tension force takes the form $\mu\boldsymbol{\nabla}\phi$. This form does not involve the gradient of the chemical potential $\boldsymbol{\nabla}\mu$, thus the results are less affected by the implementation of the boundary condition for μ (as noted above we use a simplified boundary condition for μ on immersed surfaces). The relation and difference between the two forms of interfacial tension force ($-\phi\boldsymbol{\nabla}\mu$ and $\mu\boldsymbol{\nabla}\phi$) were clearly described in [6, 23]. As to the axisymmetric LBM, most of the details can be found in [17]. It is noted that the 2-D and 3-D LBM can deal with two-phase flows with contrasts in both density and viscosity whereas the axisymmetric LBM is still unable to handle problems with density contrast. Nevertheless, as compared with that in [17], the axisymmetric LBM has been improved in two aspects in the present work: 1) it is extended for problems with viscosity contrast; 2) it is extended to handle problems with solid walls immersed inside the domain.

On an immersed solid boundary of any shape, the interpolated bounce-back method is applied for f_i according to [24]. This intuitive method obtains the unknown DF f_i at a point near a solid boundary through different spatial interpolation schemes, depending on the distance between the site and the wall boundary. Figure 5 illustrates the basic idea of *interpolated bounce-back*. For simplicity, only linear interpolation is considered here. In fig. 5, q is the distance between the point near the wall and the wall scaled by the distance between two neighbouring points along the direction under consideration. When $q < \frac{1}{2}$, the unknown DF $f_i(\boldsymbol{x}_A, t + \delta_t)$ is obtained from $f^c_{i'}(\boldsymbol{x}_D, t)$ streaming towards the wall (along the opposite direction, *i.e.*, $\boldsymbol{e}_{i'} = -\boldsymbol{e}_i$) which reaches $\boldsymbol{x}_A$ after streaming for a time step δ_t (*i.e.*, the interpolation is done first, then the streaming (including bounce-back at the wall) is carried out). The superscript c in $f^c_{i'}(\boldsymbol{x}_D, t)$ denotes the value is taken just after the collision step. When $q > \frac{1}{2}$, $f_i(\boldsymbol{x}_A, t + \delta_t)$ is obtained by interpolating the distribution functions $f_i(\boldsymbol{x}_D, t + \delta_t)$ and $f_i(\boldsymbol{x}_B, t + \delta_t)$ which are obtained as $f_i(\boldsymbol{x}_D, t + \delta_t) = f^c_{i'}(\boldsymbol{x}_A, t)$ and $f_i(\boldsymbol{x}_B, t + \delta_t) = f^c_i(x_A, t)$ (*i.e.*, the streaming (including bounce-back at the wall) is carried out first, then the interpolation is done). The detailed interpolation formula reads

$$f_i(\boldsymbol{x}_A, t + \delta_t) = \begin{cases} 2q f^c_{i'}(\boldsymbol{x}_A, t) + (1 - 2q) f^c_{i'}(\boldsymbol{x}_B, t), & \text{for } q < \dfrac{1}{2}\,, \\ \dfrac{1}{2q} f^c_{i'}(\boldsymbol{x}_A, t) + \dfrac{2q - 1}{2q} f^c_i(\boldsymbol{x}_A, t), & \text{for } q > \dfrac{1}{2}\,. \end{cases} \tag{24}$$

When $q = \frac{1}{2}$, the formula reduces to the usual bounce-back-by-link scheme. Illustrations for more general situations (including quadratic interpolations) may be easily found in [24,25]. The interpolated bounce-back method is 2nd-order accurate when linear interpolation is used (as demonstrated in [24]). It is noted that the DF f_i and the hydrodynamic variables ρ, p and $\boldsymbol{u}$ in LBM are defined at the same grid nodes as the phase-field variables ϕ and μ.

3 Results and discussions

In this section we present the numerical study of several 2-D, 3-D and axisymmetric two-phase flow problems. The first is on the shape of a droplet on a sphere with different contact angles and radii. The second is about the spreading of a drop on a flat wall embedded in the domain. The third is on capillary filling in a tube under cylindrical geometry. The fourth is on a droplet impacting on a sphere and the final one involves the interaction between a droplet and multiple objects of different sizes and contact angles. It is noted that only a half of the domain is employed in all axisymmetric simulations. The density ratio is defined as $r_\rho = \rho_L/\rho_G$, and the (kinematic) viscosity ratio is defined as $r_\nu = \nu_L/\nu_G$. The dynamic viscosity ratio is then obtained as $r_\eta = \eta_L/\eta_G = r_\rho r_\nu$. The liquid density ρ_L is taken as the reference density. In each problem, a suitable length (*e.g.*, the initial droplet radius R) is chosen as the reference length L_r. The reference velocity is derived from the interfacial tension σ and the dynamic viscosity of the liquid η_L as $U_r = \sigma/\eta_L$. From L_r and U_r, a reference time is derived as $T_r = L_r/U_r = L_r\eta_L/\sigma$. All length and time quantities are measured in

L_r and T_r respectively (unless specified otherwise). Based on these quantities, the capillary number can be calculated as $Ca = \eta_L U_r/\sigma = 1$ and the Reynolds number, $Re = \rho_L U_r L_r/\eta_L = \rho_L \sigma L_r/\eta_L^2$. In numerical simulations, the reference length L_r is discretized into N_L uniform segments and the reference time T_r is discretized into N_t uniform intervals. Thus, the grid size and time step are $\delta_x = L_r/N_L$ and $\delta_t = T_r/N_t$. In diffuse-interface simulations of binary fluids, there are two additional (numerical) parameters: the Cahn number $Cn = W/L_r$ (*i.e.*, the ratio of interface thickness over the reference length) and the Peclet number $Pe = (U_c L_c^2)/(M\sigma)$ (*i.e.*, the ratio of convection over diffusion in the CHE). The values of N_L, N_t, Cn and Pe will be given later for each problem. It is preferred to use a Cn as small as possible to approach the sharp-interface limit [6, 26] ($Cn = W/L_r = (W/\delta_x)/N_L$ should be as small as possible). Thus, for a given spatial resolution N_L, a smaller W/δ_x is preferred. However, when W/δ_x is too small, the profile of ϕ across an interface cannot be accurately captured [6]. For a given W/δ_x, a larger N_L is preferred. However, the computation cost increases quickly as N_L becomes larger for two reasons: 1) the total number of grid points increases; 2) the grid size δ_x decreases and the time step δ_t has to be also reduced (a larger N_t must be used) for stability. We set W/δ_x to be (around) 4.0 based the requirement to sufficiently resolve the profile of ϕ while keeping the computational cost reasonably low. Based on some trial studies of a case on drop spreading on a cylinder under typical numerical settings, we found that to use an even wider interface with $W/\delta_x = 5.6$ (N_L and other parameters were kept the same) did not lead to significant changes in the results as compared with $W/\delta_x = 4.0$ whereas a thinner interface with $W/\delta_x = 2.4$ produced unreliable outcomes with noticeable differences.

3.1 Droplet on a sphere

First, a droplet on a sphere is studied. The axisymmetric LBM was mainly used for this problem (for some cases, the 3-D LBM was also used). The initial radius of the droplet is R and it is chosen as the reference length L_r for this problem (*i.e.*, in the system scaled by the reference quantities, $R = 1$). In the axisymmetric simulations, the initial center of the droplet is located at $(x_{cd}, y_{cd}) = (1.5, 0)$. The solid sphere has a radius R_s and its center is fixed at $(x_{cs}, y_{cs}) = (R + R_s, 0)$. This means that the droplet initially contacts the sphere by only one point in theory. The wetting property of the outer surface of the sphere is specified by a contact angle θ_w. The size of the simulation domain is $L_x \times L_y = [1 + 2(R + R_s)] \times 2$. The Reynolds number is fixed at $Re = 100$ and the viscosity ratio is $r_\nu = 1.0$. Except for the lower boundary, stationary wall was assumed for all the other boundaries. In equilibrium, the droplet covers part of the sphere surface with the configuration determined by R, R_s and θ_w. Figure 6 shows the equilibrium configuration with the relevant quantities (R_e, α, β, l_c and h_e) illustrated clearly. Note that fig. 6 has to be rotated by 90° in the anti-clockwise direction

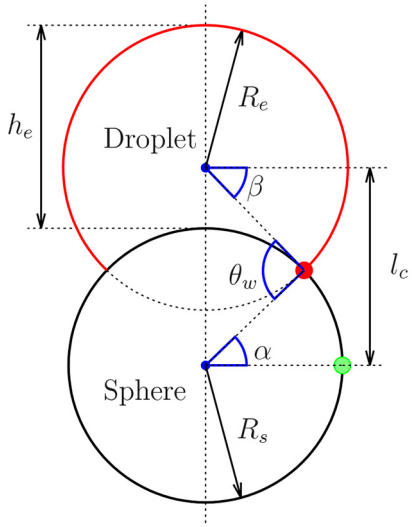

Fig. 6. The equilibrium configuration for a droplet on a solid sphere with the contact angle of the outer surface being θ_w. The surface of the droplet is part of a sphere with a radius R_e. The definitions of the two angles α and β are as illustrated. The angles satisfy $\theta_w = \alpha + \beta$. Note that $\alpha \in [-\frac{\pi}{2}, \frac{\pi}{2}]$ is positive in this figure, and it becomes negative when the intersection point (the red dot) moves beyond the green dot.

in order to match the present setup. When the droplet does not evaporate and its volume keeps unchanged, one has the following relation because of the conservation of droplet volume:

$$\frac{4}{3}\pi R_e^3 - \left[\frac{1}{3}\pi R_e^3(2 - 3\sin\beta + \sin^3\beta) + \frac{1}{3}\pi R_s^3(2 - 3\sin\alpha + \sin^3\alpha)\right] = \frac{4}{3}\pi R^3. \quad (25)$$

The right-hand side of eq. (25) represents the initial drop volume (a whole sphere of radius R), and the left hand side of eq. (25) represents the final drop volume which is obtained by subtracting the two spherical caps (one is part of the red sphere of radius R_e and the other is part of the black sphere of radius R_s) from the red sphere. The volumes of the spherical caps can be calculated directly by integration or according to the formula in [27]. Because $R_e \cos\beta = R_s \cos\alpha$ and $\beta = \theta_w - \alpha$, the following equation can be derived for the unknown angle α:

$$f(\alpha) = \cos^3\alpha[2 + 3\sin(\theta_w - \alpha) - \sin^3(\theta_w - \alpha)] - \cos^3(\theta_w - \alpha)[(2 - 3\sin\alpha + \sin^3\alpha) + 4(R/R_s)^3] = 0. \quad (26)$$

Once α is found by solving eq. (26), the angle β and the radius of the droplet R_e are easily obtained. The distance between the two centers can be calculated as $l_c = R_e \sin\beta + R_s \sin\alpha$, and the height of the droplet on the axis is found as $h_e = R_e + l_c - R_s$.

Two series of tests were performed with $Pe = 10000$. In one of them, the radius of the sphere R_s was fixed to be 1 and the contact angle θ_w varied from 30° to 150°

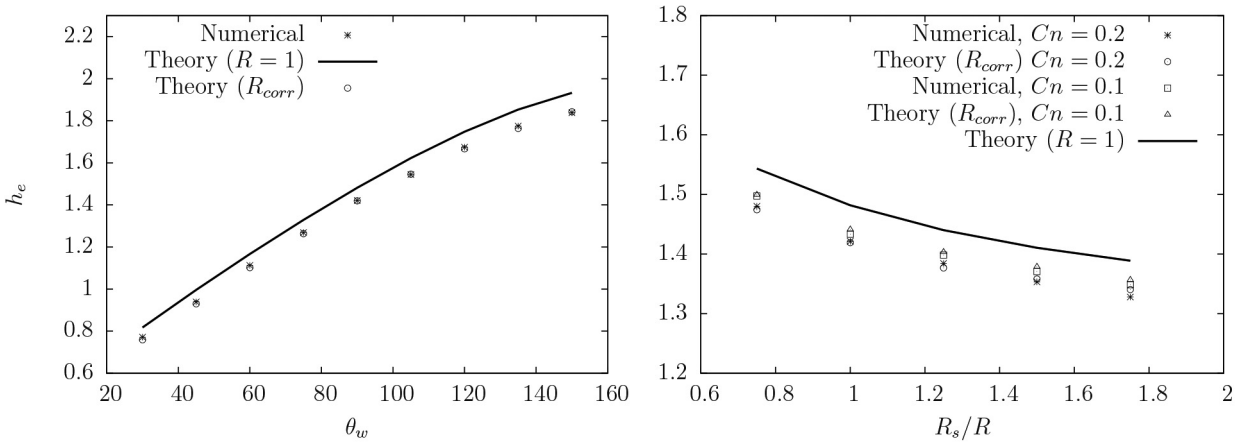

Fig. 7. Variations of the droplet height in equilibrium h_e with the contact angle of the sphere θ_w and the ratio of the radius of sphere over the initial drop radius R_s/R. For the left panel, R_s is fixed to be 1, and the shared simulation parameters are: $N_L = 20$, $N_t = 200$, $Cn = 0.2$. For the right panel, θ_w is fixed to be 90°, and two sets of simulation parameters with different resolutions are used: 1) $N_L = 20$, $N_t = 200$, $Cn = 0.2$; 2) $N_L = 40$, $N_t = 400$, $Cn = 0.1$.

($Cn = 0.2$, $N_L = 20$ for this series); in the other, θ_w was fixed to be 90° and R_s varied from 0.75 to 1.75 (two sets of simulations with $Cn = 0.2$, $N_L = 20$ and $Cn = 0.1$, $N_L = 40$ were done for this series). In all cases of both series, the interface thickness W/δ_x is 4 lattice nodes. The radius of the sphere R_s is resolved by 15 nodes minimally (for $R_s = 0.75$ and $N_L = 20$) and 70 nodes maximally (for $R_s = 1.75$ and $N_L = 40$). Figure 7 compares the variations of the droplet height h_e with the contact angle θ_w and the ratio R_s/R by numerical simulations and by eq. (26) for the two series of tests. Note that during the simulation the droplet volume decreased to some extent which is a natural consequence of the diffuse-interface model. This shrinkage of the droplet is affected by the Cahn number Cn and the ratio of the initial droplet volume over that of the whole domain (denoted as V_d/V_{wd}), and the speed of the shrinkage process is affected by the Peclet number Pe [28]. When the initial droplet radius (which is always taken to be $R = 1$) is used in eq. (26), the droplet height h_e predicted by the theory is larger than that obtained numerically, as found in fig. 7 for all cases. At the same time, it is seen that the deviations are not very significant and the trends by both numerical and theoretical solutions agree with each other. We also tried replacing R in eq. (26) with another radius R_{corr} which was determined based on the droplet volume at the end of simulation, say, $V_{d,e}$, as $R_{corr} = (V_{d,e}/V_d)^{1/3}$. As found from fig. 7, h_e predicted by eq. (26) using R_{corr} is much closer to the numerical predictions than that using $R = 1$. From the right panel of fig. 7, it is observed that when Cn decreases from 0.2 to 0.1 (N_L increases from 20 to 40), the numerical results become closer to the theoretical prediction using $R = 1$. The reason is that the shrinkage of droplet is less severe at $Cn = 0.1$. We wound like to note that the problem of droplet shrinkage is much more severe in axisymmetric (actually 3-D) simulations than in 2-D ones when other parameters are the same. The ratio of the droplet volume over that of the whole domain V_d/V_{wd} is $\frac{V_d}{V_{wd}}|_{2-D} = (\frac{1}{2}\pi R^2)/(L_x L_y)$ in 2-D whereas it becomes $\frac{V_d}{V_{wd}}|_{3-D} = (\frac{2}{3}\pi R^3)/(\pi L_y^2 L_x) = (\frac{4}{3\pi}\frac{R}{L_y})\frac{V_d}{V_{wd}}|_{2-D}$ under the axisymmetric setup. According to [28], the relative decrease of the droplet radius in 2-D and 3-D may be estimated as

$$\left.\frac{\delta R}{R}\right|_{2-D} = -\frac{\sqrt{2}}{24}\left(\frac{V_{wd}}{V_d}\right)\left(\frac{W/(2\sqrt{2})}{R}\right),$$
$$\left.\frac{\delta R}{R}\right|_{3-D} = -\frac{\sqrt{2}}{18}\left(\frac{V_{wd}}{V_d}\right)\left(\frac{W/(2\sqrt{2})}{R}\right), \tag{27}$$

where δR is the absolute change of the droplet radius, and $W/(2\sqrt{2})$ is the interface thickness defined therein. Thus, we have $\frac{\delta R}{R}|_{3-D}/\frac{\delta R}{R}|_{2-D} = \frac{3\pi}{4}\frac{L_y}{R}\frac{24}{18} = \pi\frac{L_y}{R}$. For the present case $L_y = 2R$, one has $\frac{\delta R}{R}|_{3-D}/\frac{\delta R}{R}|_{2-D} = 2\pi$. This means that the shrinkage of the droplet in an axisymmetric simulation using $L_y = 2R$ is more than *six times* more severe than that in the corresponding 2-D one using the same Cahn number Cn and domain size $L_x \times L_y$. Therefore, it is recommended to take into account the effect of droplet shrinkage when making comparisons between the numerical and analytical predictions here (unless Cn is small enough). Besides the droplet height h_e, we also examined the interface shapes at the end of the simulations for four cases (two for each series: $\theta_w = 45°$ and 135° at $R_s = 1$, $Cn = 0.2$, and $R_s = 0.75$ and 1.5 at $\theta_w = 90°$, $Cn = 0.1$). Figure 8 plots the contour lines of ϕ for these four cases. It is seen that the final shapes agree well with the theoretical predictions for all the four cases at different contact angles and radii of the sphere. These results suggest that using the present improved method one can calculate the equilibrium interface shape on a curved surface accurately in the cylindrical coordinate.

In the above, the minimum R_s is 0.75 (for the smallest $N_L = 20$, R_s is resolved by 15 lattice nodes). One might be curious on what happens when R_s becomes even smaller. We also tried 0.6 and 0.1 for R_s with $Cn = 0.2$

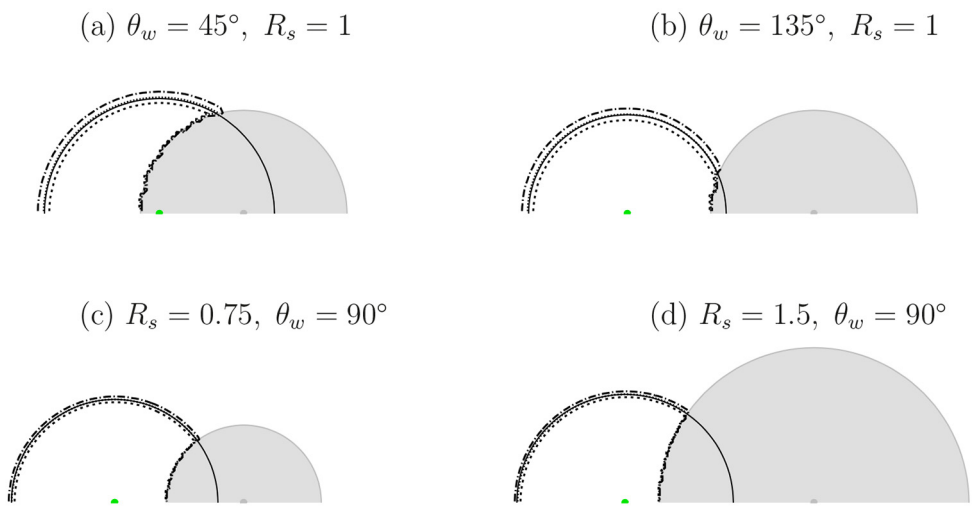

Fig. 8. Equilibrium shapes of a droplet on a sphere with the following parameter settings: (a) $\theta_w = 45°$, $R_s = 1$, $Cn = 0.2$; (b) $\theta_w = 135°$, $R_s = 1$, $Cn = 0.2$; (c) $R_s = 0.75$, $\theta_w = 90°$, $Cn = 0.1$; (d) $R_s = 1.5$, $\theta_w = 90°$, $Cn = 0.1$. The shaded part denotes the sphere. The three parallel lines are the contour lines for $\phi = -0.5$, 0, and 0.5. The solid circle partly penetrating into the sphere represents the theoretical prediction using the corrected droplet radius R_{corr} (the small green dot denotes its center).

and $N_L = 20$ ($W/\delta_x = 4$). For $R_s = 0.1$, the number of lattice nodes to resolve it was only 2. Intuitively, one may expect that, when this number is very small, the basic assumption that the surface can be considered as flat at the grid level is violated and some error may be incurred. However, the actual performance of the present method was surprisingly well. Figure 9 shows the interface shapes in equlibrium for different radii ($R_s = 0.6$ and 0.1) and contact angles ($\theta_w = 90°$ and 60°) of the sphere together with the theoretical predictions obtained using R_{corr} at the end of simulation. It is seen from fig. 9 that for all four cases the numerical results agree well with the theoretical results. When $R_s = 0.6$, the droplet heights h_e by simulation are 1.516 and 1.267 for $\theta_w = 90°$ and 60°, respectively, whereas the theoretical predictions are 1.519 and 1.269. When $R_s = 0.1$, $h_e = 1.812$ and 1.744 for $\theta_w = 90°$ and 60°, whereas theoretical predictions are 1.819 and 1.769. It is seen that when R_s (the number of nodes to resolve R_s) decreases, the deviation from theoretical results increases, but remains to be quite small. One possible reason for this good performance at a relatively low resolution of a curved surface could be the use of LBM and the isotropic discretization scheme based on the lattice velocity model. For example, the D2Q9 model involves eight neighbouring nodes and the information on how a surface intersects the eight links is used in our simulations.

In addition to the above axisymmetric simulations, some preliminary studies on 3-D droplet spreading on a sphere were also carried out. The initial center of the droplet of radius $R = 1$ is located at $(x_{cd}, y_{cd}, z_{cd}) = (0, 0, 3.1)$. The solid sphere has a radius $R_s = 1$ and its center is fixed at $(x_{cs}, y_{cs}, z_{cs}) = (0, 0, 1.1)$. It is noted that due to the symmetry of this problem, only a quarter of the domain is used. The size of the simulation domain is $L_x \times L_y \times L_z = 2 \times 2 \times 4.5$. Symmetric boundary conditions are applied for the x-z planes at $y = 0$ and $y = 2$,

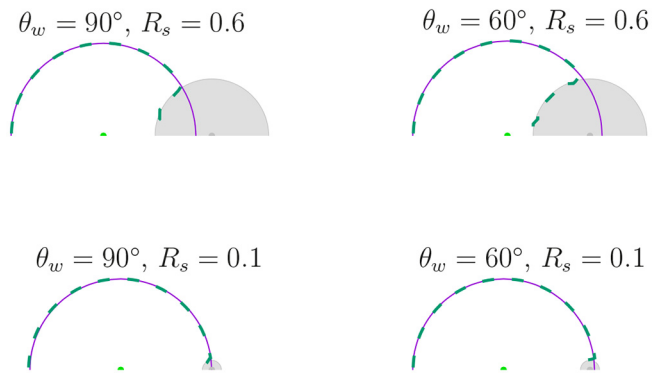

Fig. 9. Snapshots of the interface for a droplet on a sphere in equilibrium for different radii and contact angles of the sphere. The theoretical predictions are plotted in solid lines and the numerical results are in dashed lines. The shaded part denotes the sphere.

and also for the y-z planes at $x = 0$ and $x = 2$. Wall boundary conditions are applied for the two x-y planes at $z = 0$ and $z = 4.5$. The Reynolds number is $Re = 100$ and the kinematic viscosity ratio is fixed at $r_\nu = 1$. Some shared parameters are $N_L = 32$, $N_t = 192$, $Cn = 0.125$, and $Pe = 8000$. The interface thickness W/δ_x is 4 lattice nodes. The radius of the sphere R_s is resolved by 32 nodes. First the density ratio is fixed at $r_\rho = 1$ and two values for the contact angle θ_w of the sphere's outer surface were tested: $\theta_w = 60°$ and 120°. For this problem, we also performed corresponding axisymmetric simulations with a domain size $L_x \times L_y = 4.5 \times 2$ in which slip boundary conditions are used for the boundary at $y = 2$. Figure 10 compares the interfaces in the x-z plane at $y = 0.5\delta_x$ with those by the axisymmetric simulations at $t = 0, 10, 25, 100$. It is seen that the 3-D results agree well with the axisymmetric ones. The 3-D snapshots for

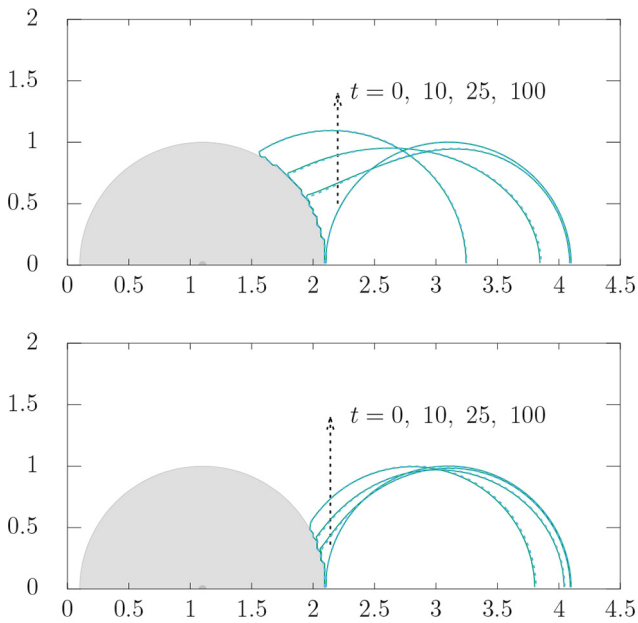

Fig. 10. Evolutions of the interface in the x-z plane at $y = 0.5\delta_x$ in the 3-D simulation of droplet spreading on a sphere and those in the corresponding axisymmetric simulation for $\theta_w = 60°$ (upper panel) and $\theta_w = 120°$ (lower panel). The selected times are $t = 0, 10, 25, 100$ (along the direction of the arrow). The shaded part denotes the sphere. The axisymmetric results are plotted in solid lines and the 3-D ones are in dashed lines. The shared parameters are $r_\rho = 1$, $r_\nu = 1$, $Cn = 0.125$, $Pe = 8000$, $N_L = 32$, $N_t = 192$, $Re = 100$.

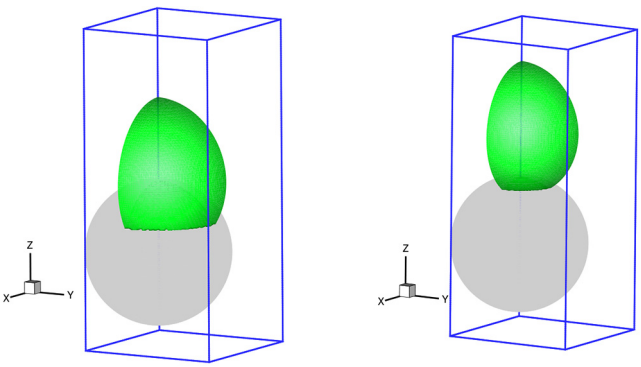

Fig. 11. Snapshots of a 3-D droplet on a sphere at $t = 100$ with the following parameter settings: (a) $\theta_w = 60°$ (left panel); (b) $\theta_w = 120°$ (right panel). The shaded part denotes the sphere.

the two cases at $t = 100$ (when the droplet almost becomes static on the sphere) are shown in fig. 11 from which the difference caused by different wettabilities is clearly seen. Based on the above results, the implementation of the present method in 3-D is verified. As mentioned above, the 3-D LBM can deal with problems with density contrast. We also simulated another case with $r_\rho = 10$ and $\theta_w = 60°$ to investigate the effects of density ratio on the droplet spreading. This case cannot be handled by the axisymmetric LBM yet. Figure 12 compares the evolutions of the

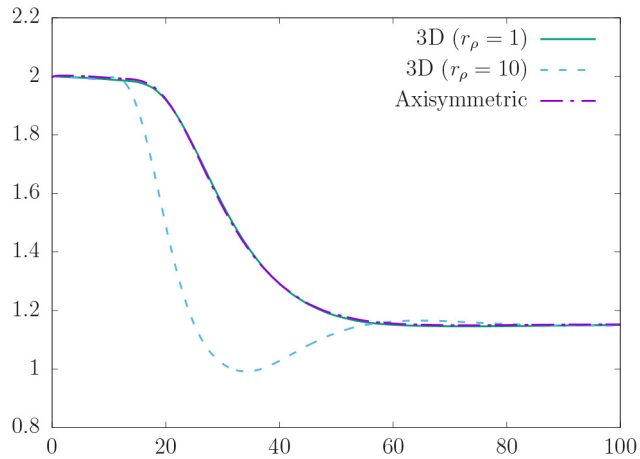

Fig. 12. Evolutions of the height of the droplet along the axis H_z in the 3-D simulation of droplet spreading on a sphere at $r_\rho = 1$ and $r_\rho = 10$. The axisymmetric results are also shown for reference. The shared parameters are $\theta_w = 60°$, $r_\nu = 1$, $Cn = 0.125$, $Pe = 8000$, $N_L = 32$, $N_t = 192$, $Re = 100$.

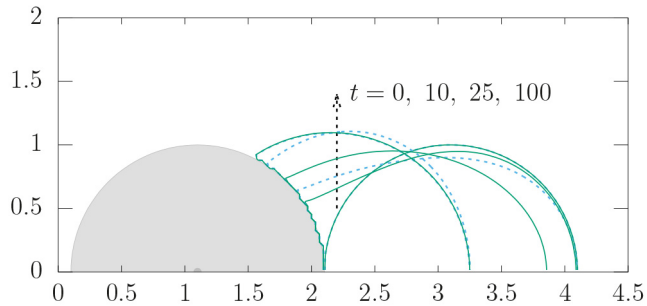

Fig. 13. Evolutions of the interface in the x-z plane at $y = 0.5\delta_x$ in the 3-D simulation of droplet spreading on a sphere. The selected times are $t = 0, 10, 25, 100$ (along the direction of the arrow). The shaded part denotes the sphere. The results at $r_\rho = 1$ are plotted in solid lines and those at $r_\rho = 10$ are in dashed lines. The shared parameters are $\theta_w = 60°$, $r_\nu = 1$, $Cn = 0.125$, $Pe = 8000$, $N_L = 32$, $N_t = 192$, $Re = 100$.

height of the droplet H_z along the z-axis in the 3-D simulations for $r_\rho = 1$ and $r_\rho = 10$. Figure 13 compares the interfaces in the x-z plane at $y = 0.5\delta_x$ at $t = 0, 10, 25, 100$ for the two cases at different density ratios. It can be observed from figs. 12 and 13 that at $r_\rho = 10$ the droplet spreads faster and H_z shows an "overshoot" during the spreading process before it reaches an equilibrium value. Figure 14 shows the snapshots of the droplet at $t = 30$ for $r_\rho = 1$ and $r_\rho = 10$. It is obvious that the droplet spreads further on the droplet at this moment when $r_\rho = 10$. As compared to the case with $r_\rho = 1$, the surrounding gas density is only one-tenth. Thus, the droplet experiences less drag and spreads faster when $r_\rho = 10$. Nevertheless, the final shapes at $t = 100$ for the two cases are almost the same (see fig. 13) because the equilibrium shape is determined by the contact angle and not affected by the density. Note that in fig. 12 the evolution of the droplet

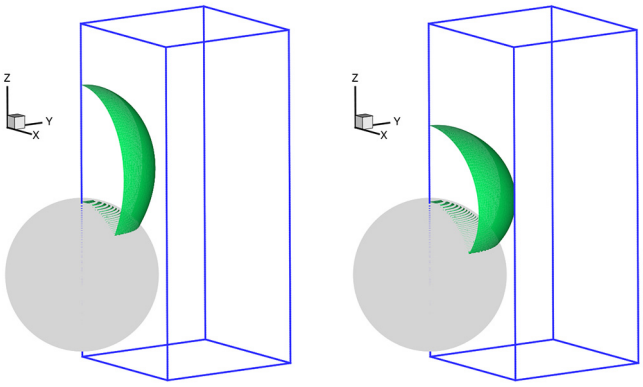

Fig. 14. Snapshots of a 3-D droplet on a sphere at $t = 30$ for (a) $r_\rho = 1$ (left panel) and (b) $r_\rho = 10$ (right panel). The shaded part denotes the sphere. The shared parameters are $\theta_w = 60°$, $r_\nu = 1$, $Cn = 0.125$, $Pe = 8000$, $N_L = 32$, $N_t = 192$, $Re = 100$.

height by the corresponding axisymmetric simulation with $r_\rho = 1$ was also plotted and the agreement between the 3-D and axisymmetric simulations is again confirmed.

3.2 Drop spreading on an embedded inclined wall

Next, we investigate the spreading of a drop on a wall placed inside the fluid domain at a given angle of inclination α. The 2-D LBM was employed. We used $r_\rho = 10$ and $r_\nu = 0.25$ for this problem. The wall is represented by a straight line segment between two points at $(x_{s,l}, y_{s,l})$ and $(x_{e,l}, y_{e,l})$. Two values of α were tried: $\alpha = 4.086°$ and $12.095°$ ($\tan\alpha = 1/14$ and $3/14$). The start point was fixed at $(x_{s,l}, y_{s,l}) = (0.5, 0.5)$ whereas $(x_{e,l}, y_{e,l}) = (7.5, 1.0)$ was used for $\alpha = 4.086°$, and for $\alpha = 12.095°$, $(x_{e,l}, y_{e,l}) = (7.5, 2.0)$. The contact angle on this immersed wall is $\theta_w = 60°$. The domain size is 8×4.5. Periodic boundary conditions are applied at all four domain boundaries. It is noted that gravity effects are not included in this problem and the spreading is purely driven by interfacial tension forces. For comparison, we also carried out another simulation using the characteristic interpolation (CI) given in [10]. In the simulation using the original CI, the problem is symmetric about the x-axis and only the upper half of the domain is used (the domain size for simulation is 4×4); except for the bottom boundary, the boundary conditions for a static wall are applied at the other three boundaries. Figure 15 illustrates the initial setups of the two different simulations. The left figure is for the simulation using the original CI, and the right is for the current simulation. The small red dot at (x'_0, y'_0) in the right panel denotes the initial point of contact between the drop and the wall. In the simulation at $\alpha = 4.086°$, the initial drop center (x_{cd}, y_{cd}) is located at $(3.9288, 1.7475)$, and the contact point is at $(x'_0, y'_0) = (4, 0.75)$. In the simulation at $\alpha = 12.095°$, $(x_{cd}, y_{cd}) = (3.7905, 2.2278)$, and $(x'_0, y'_0) = (4, 1.25)$. It is also noted that the drop spreading studied here is relatively slow and the boundaries of the domain have little effect on the spreading process. Some shared computational parameters are $N_L = 32$, $N_t = 128$, and $Cn = 0.125$. In all cases the interface thickness W/δ_x is 4 lattice nodes. Figure 16 compares the evolutions of the interface by the simulation using CI and the current simulations at the two inclination angles. Note that in order to compare the interface shapes, the coordinates in the current simulations have been transformed as $x = (x' - x'_0)\cos\beta + (y' - y'_0)\sin\beta$, $y = -(x' - x'_0)\sin\beta + (y' - y'_0)\cos\beta$, where $\beta = \alpha + \frac{\pi}{2}$. It is found from fig. 16 that at both values of α the differences between the present interface shapes and those using CI are quite small at all times. This means that the proposed method can be used to simulate dynamic problems involving contact line movement with the outcomes matching the corresponding simulations using the original CI.

3.3 Capillary filling

The third problem is on the dynamics of capillary filling in a tube. The axisymmetric LBM was used for this study. Previously, capillary filling in a 2-D channel was investigated by the LBM [29,30] and the results were compared with Washburn's law (its integral form) [31]. Here we study the capillary filling in a tube under cylindrical geometry, which is closer to the setup originally considered by Washburn [31]. The present case is in a closed space and gravity is neglected. The initial setup is shown in fig. 17. The fluid that penetrates into the tube is "liquid" (with $\phi = 1$) and the other fluid is "gas" (with $\phi = -1$) (they actually have the same density in the present simulations). For this problem, the tube diameter D (at the exit) is chosen as the characteristic length L_c. The size of the domain is $L_x \times L_y = 8 \times 3$. The tube wall is represented by a straight line segment immersed in the domain. The start point of the line segment was at $(x_{s,l}, y_{s,l})$ and it ends at $(x_{e,l}, y_{e,l}) = (7.0, 0.5)$. The contact angle of the inner surface of the tube is θ_{w1} and that of its outer surface is θ_{w2}. The contact angle of the upper boundary of the domain θ_{w3} is fixed at 90°. Initially, a liquid film having a width of $H = 2$ is specified and the tube is submerged in the liquid with a depth $l_0 = 1$. The kinematic viscosity ratio is $r_\nu = 80$. Thus, the viscous dissipation in the "gas" is much smaller (so as to conform to the assumption made in Washburn's derivation). For a straight tube, assuming the flow inside the tube follows Poiseuille's law and neglecting any slip on the wall, one can derive the following relation for the speed of interface v_{if} [31]:

$$v_{if} = \frac{\mathrm{d}l}{\mathrm{d}t} = \frac{\sum Pr^2}{8\eta_L l}, \tag{28}$$

where l is the length of penetration, $\sum P$ is the total driving pressure, $r = D/2$ is the tube radius and η_L is the dynamic viscosity of the liquid. Since neither the atmospheric pressure nor the gravity are considered, the total driving pressure is given by $\sum P = 2\sigma\cos\theta_d/r$ where θ_d is the dynamic contact angle of the moving interface. Using the characteristic length $L_c = D$ and the characteristic velocity $U_c = \sigma/\eta_L$ and substituting the total driving

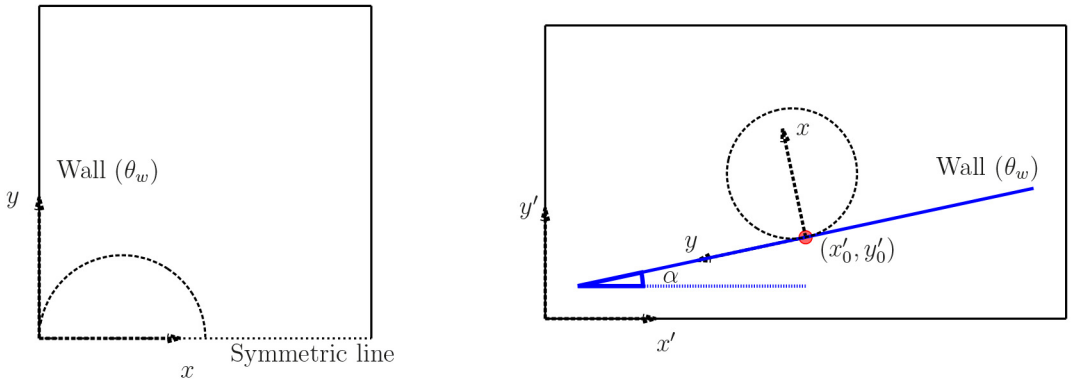

Fig. 15. Initial setups for the drop spreading problem by two types of simulations. Left: a drop spreading on the left wall where the original characteristic interpolation is applied; right: a drop spreading on the wall embedded inside the domain with an inclination angle α on which the proposed method is applied. The dashed line represents the initial interface (the contour line for $\phi = 0$). The solid blue line represents the wall.

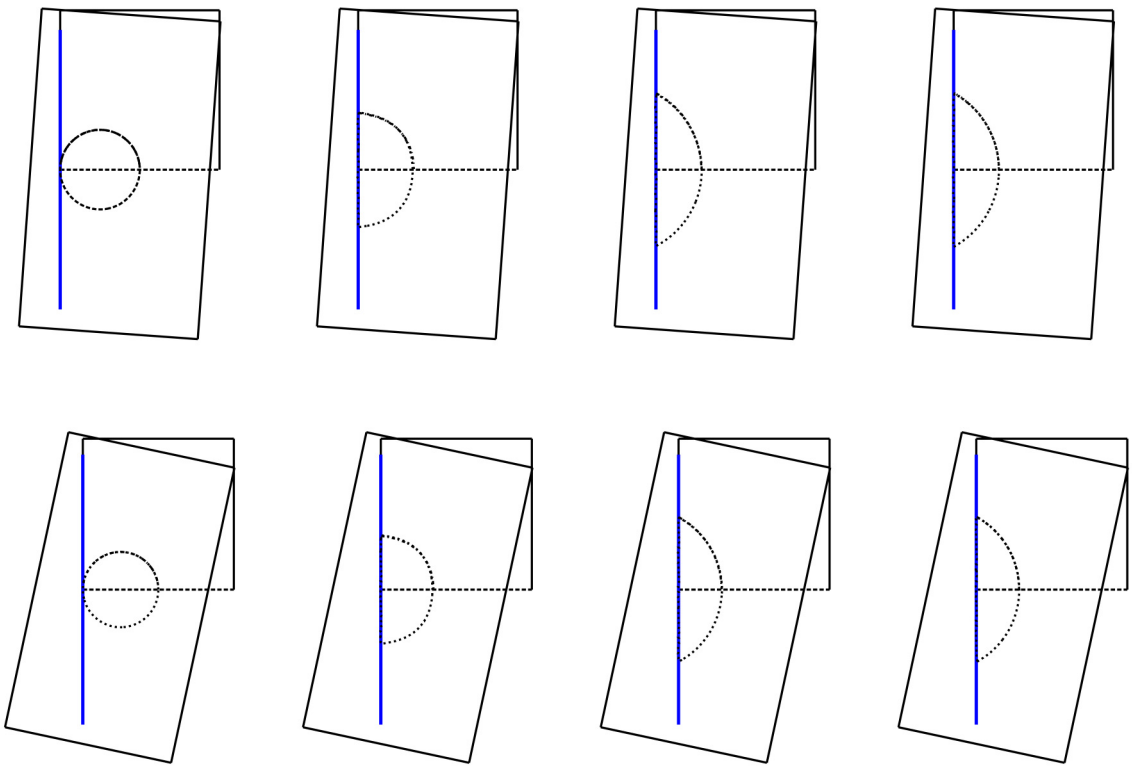

Fig. 16. Snapshots of the interfaces at $t = 0$, 20, 40, and 60 (from left to right) by two types of simulations with one overlaid on the other. For the simulations using the proposed method, the angle of inclination is $\alpha = 4.086°$ in the upper row and $\alpha = 12.095°$ in the lower row. Some shared parameters for the simulations are $r_\rho = 10$, $r_\nu = 0.25$, $Cn = 0.125$, $N_L = 32$, $N_t = 128$, $Re = 100$.

pressure with $2\sigma \cos\theta_d/r$, one can rewrite eq. (28) as

$$\frac{v_{if}}{U_c} = \frac{\cos\theta_d}{8(l/L_c)} \,. \tag{29}$$

In our simulations, the Reynolds number is quite low ($Re = 1$) in order to neglect the inertial effect (not considered by Washburn either). The interface velocity in the tube v_{if} at time step n is calculated as $v_{if}^n = (x_{if}^n - x_{if}^{n-1})/\delta_t$ where x_{if}^n and x_{if}^{n-1} are the interface positions along the axis at time step n and $n-1$. In all cases the interface thickness W/δ_x is 4 lattice nodes. In the first series of simulations, the shared parameters are: $(x_{s,l}, y_{s,l}) = (1.0, 0.5)$, $\theta_{w2} = 90°$, $Cn = 0.125$, $Pe = 8000$, $N_L = 32$, $N_t = 2560$. Since $y_{s,l} = y_{e,l} = 0.5$, the tube wall is parallel to the axis (*i.e.*, it is a straight tube). Figure 18 shows the evolutions of the interface velocity v_{if} for two values of the inner contact angle: $\theta_{w1} = 75°$ and $60°$. Also

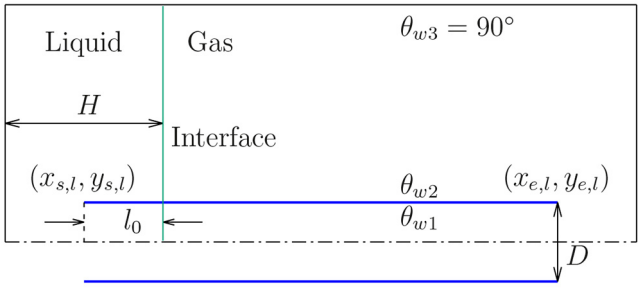

Fig. 17. Initial setup for the capillary filling in a tube.

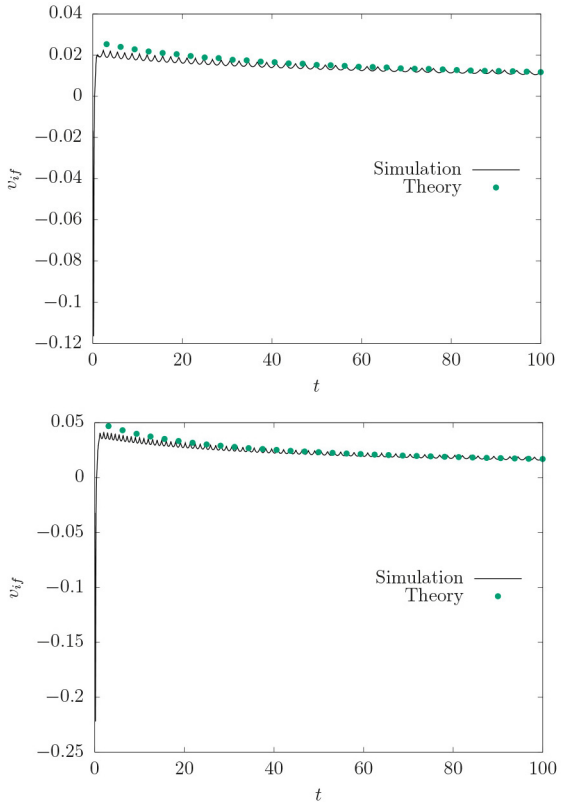

Fig. 18. Evolution of the interface velocity in the tube during the filling process for (a) $\theta_{w1} = 75°$ (upper panel) and (b) $\theta_{w1} = 60°$ (lower panel). Some shared parameters for the simulations are $r_\nu = 80$, $Cn = 0.125$, $Pe = 8000$, $N_L = 32$, $N_t = 2560$, $Re = 1$.

shown in fig. 18 are the predictions by eq. (29) with the dynamic contact angle θ_d extracted by fitting the interface with an arc (similar to [29]). One can see from fig. 18 that initially the interface velocity is negative and has a large magnitude. This reflects the initial adjustment due to the difference between the initial configuration (corresponding to a contact angle of 90°) and that as required by the specified contact angle θ_{w1}. After this stage, v_{if} soon becomes positive and seems to gradually become quasi-steady though small oscillations in it persist throughout the simulation. Such oscillations are caused by the "grid roughness effect" which was analyzed in [6,32] (it is hard to fully eliminate it and we shall not focus on it here). Neglecting such small oscillations, one can see that the interface velocity agrees with the theoretical predictions better and better as time progresses for both $\theta_{w1} = 75°$ and 60°. After more careful examination one finds that v_{if} actually decreases slowly in the quasi-steady stage. This is likely due to the finite domain used here. If the liquid reservoir is infinitely large and the tube is infinitely long, the interface velocity v_{if} should reach a constant after some time. It is noted that the dynamic contact angle θ_d was extracted at each time step and it evolved in a way similar to v_{if} (*i.e.*, it experiences an initial adjustment stage and then a quasi-steady stage). At the end of simulation ($t = 100$), $\theta_d \approx 76.9°$ for $\theta_{w1} = 75°$ and $\theta_d \approx 63.6°$ for $\theta_{w1} = 60°$. In addition to the straight tube, a slightly tapered tube with $(x_{s,l}, y_{s,l}) = (1.0, 0.75)$ was also tested. The angle between the tube wall and the x-axis is about 2.4°. The contact angle of the outer surface is set as $\theta_{w2} = 87.6°$ so that the interface outside the tube remains nearly flat. The inner contact angle is still $\theta_{w1} = 75°$. All other parameters are the same. Figure 19 shows the interfaces at $t = 0$, 25, 50, 75 and 100 for the straight tube and the tapered tube. From fig. 19 one can observe that the filling process is much faster in the tapered tube even though it is only slightly tapered. This is caused by the combined effects of the specific geometry and the inner contact angle. In fact, for the tapered tube the filling still occurs even when the inner contact angle is set as $\theta_{w1} = 90°$ (the results are not given here for brevity). After more detailed examination, we found that the interface velocity v_{if} and the dynamic contact angle θ_d no longer follows eq. (29) for the tapered tube. This is not unexpected as the velocity profile inside the tapered tube deviates more from Poiseuille's law.

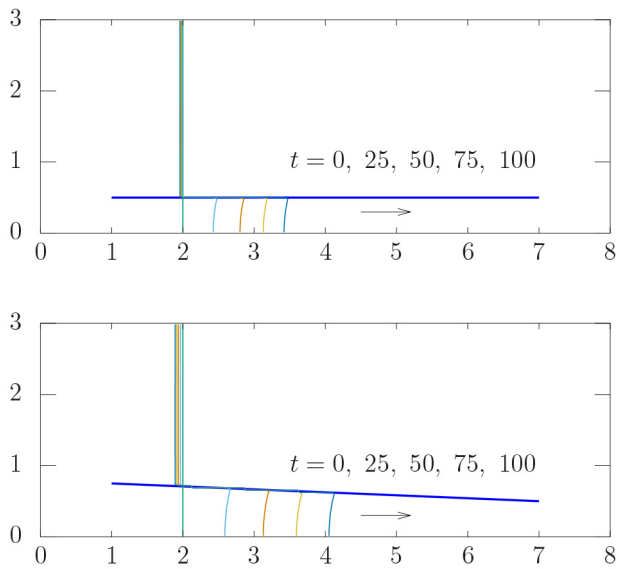

Fig. 19. Snapshots of the interface during the filling process at several selected times for (a) $(x_{s,l}, y_{s,l}) = (1.0, 0.5)$, $\theta_{w2} = 90°$ (upper panel) and (b) $(x_{s,l}, y_{s,l}) = (1.0, 0.75)$, $\theta_{w2} = 87.6°$ (lower panel). Some shared parameters for the simulations are $\theta_{w1} = 75°$, $r_\nu = 80$, $Cn = 0.125$, $Pe = 8000$, $N_L = 32$, $N_t = 2560$, $Re = 1$.

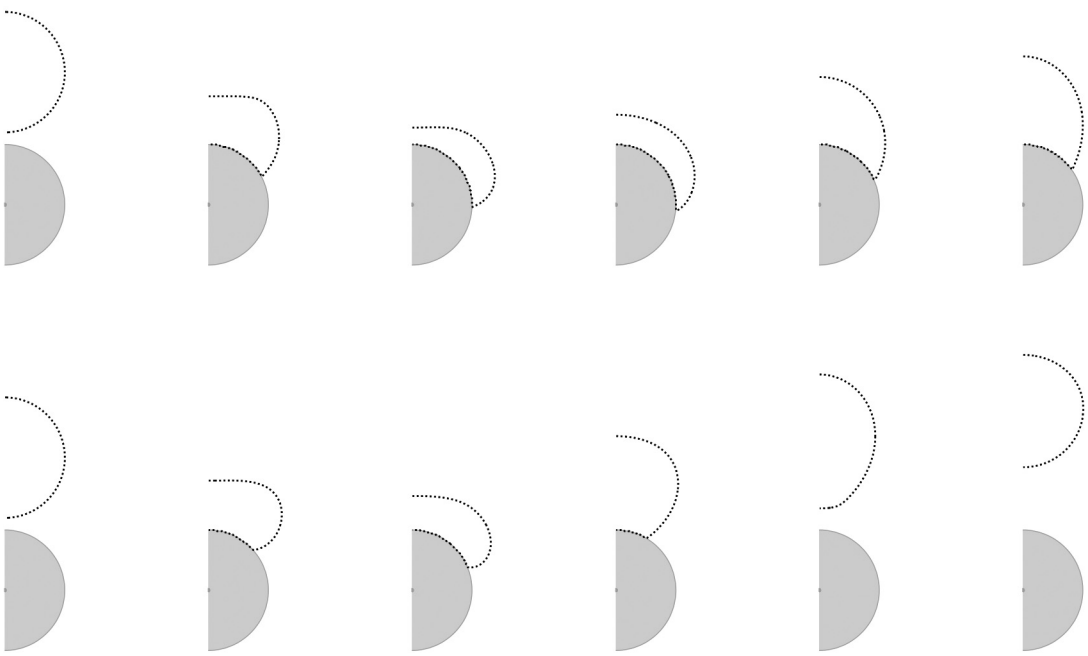

Fig. 20. Snapshots of a droplet impacting on a sphere at $We_{imp} = 10$, $Re_{imp} = 100$, $r_\nu = 10$ and $R_s = 1$. The upper row is for $\theta_w = 60°$ and the lower is for $\theta_w = 120°$. From left to right, the times (scaled by T_{imp}) are 0, 1, 2, 4, 6, and 8. The dashed line represents the interface where $\phi = 0$ and the figures are rotated by 90° in the clockwise direction so that the x-axis points downwards. This rotation applies for figs. 21, 22 and 23 as well.

3.4 Droplet impact on a sphere

The fourth problem is on the droplet impact on a sphere at a given velocity. The axisymmetric LBM was used. For this problem, we define the impact Reynolds and Weber numbers based on the impact velocity U_{imp} and the initial droplet diameter $D = 2R$ as [33]

$$Re_{imp} = \frac{\rho U_{imp} D}{\eta_L}, \qquad We_{imp} = \frac{\rho U_{imp}^2 D}{\sigma}. \tag{30}$$

The setup is similar to the first problem in the above except that initially the droplet is put slightly away from the sphere with the distance between their centers being $R_s + 1.2R$. We also introduce a characteristic time $T_{imp} = D/U_{imp}$ for this problem. The shared parameters for all cases are $We_{imp} = 10$, $L_x \times L_y = 8 \times 4$, $N_L = 50$, $N_t = 500$, $Cn = 0.08$, $Pe = 15625$. The interface thickness W/δ_x is 4 lattice nodes. The radius of the sphere R_s is resolved by 35 nodes minimally (for $R_s = 0.7$) and 50 nodes maximally (for $R_s = 1$). It is noted that in real world the symmetry about the axis for the problem of droplet impact on a sphere is likely to be broken when the Weber number becomes larger. This is because small disturbances tend to grow instead of being damped when inertial effects are more dominant than surface tension effects.

First, four cases were studied with the contact angle of the sphere θ_w being 60° and 120° and the impact Reynolds number Re_{imp} being 100 and 1000. The viscosity ratio is fixed at $r_\nu = 10$ and the radius of the sphere is fixed at $R_s = 1$. Figure 20 shows the evolutions of the interfaces at $\theta_w = 60°$ and 120° for $Re_{imp} = 100$. For both cases the droplet undergoes some deformation and spreads on the sphere initially. When the sphere surface is more wettable ($\theta_w = 60°$), the droplet spreads further on the sphere. After reaching a maximum, it begins to retract and eventually stays on the sphere. In contrast, when the sphere surface is less wettable ($\theta_w = 120°$), the retraction process keeps going on and the droplet finally rebounds from the sphere. With a much higher impact velocity (Reynolds number), things may be different. The snapshots of the interfaces at $Re_{imp} = 1000$ for $\theta_w = 60°$ and 120° are given in fig. 21. When Re_{imp} is ten folds larger, the interface evolution for $\theta_w = 120°$ is similar to that at $Re_{imp} = 100$, but for $\theta_w = 60°$ the situation is completely different: at some time the droplet breaks into a ring covering part of the sphere, this ring spreads over the sphere while moving towards the other end, and then it reconnects with itself and forms a droplet again. The observations at this high Reynolds number for both $\theta_w = 60°$ and 120° are similar to those reported in [11] (see figs. 19 and 20 therein). At the same time, there are also some differences between the present results and theirs. In [11] some small satellite droplets were seen whereas they are not observed here. This could be likely due to the different density ratios used (in their simulation, the density of the droplet was a thousand times of the ambient fluid).

Next, another two cases with $\theta_w = 60°$ are studied to examine the effects of the viscosity ratio and the size of the sphere. In one case, the viscosity ratio r_ν is changed to 0.1 while the impact Reynolds number is $Re_{imp} = 1000$. In the other, the radius of the sphere R_s is changed to

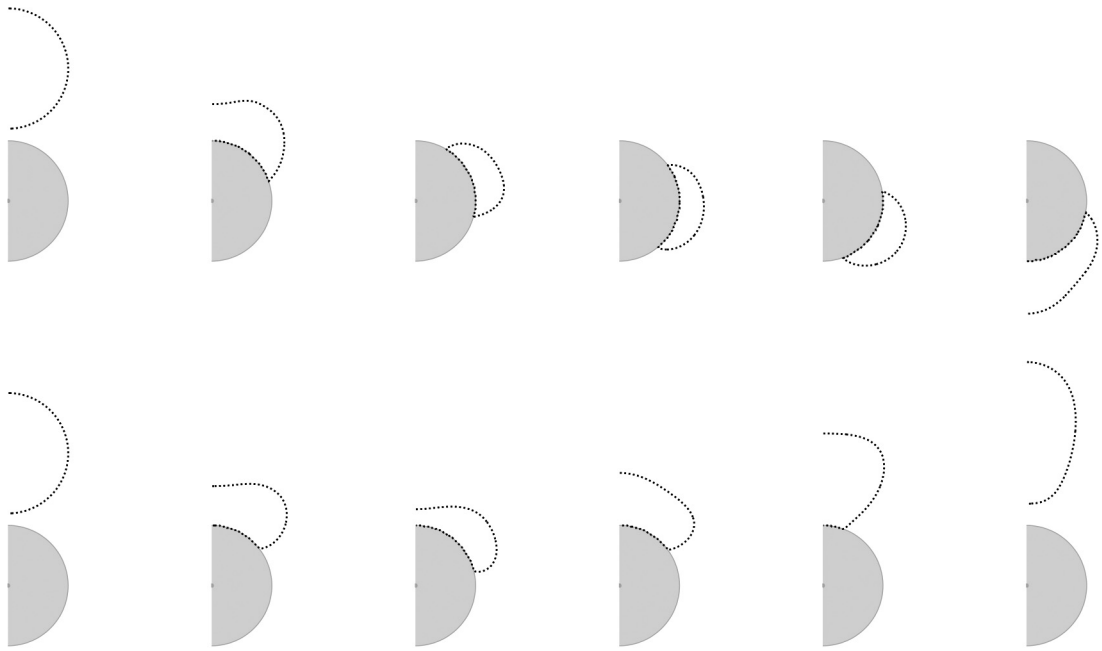

Fig. 21. Snapshots of a droplet impacting on a sphere at $We_{imp} = 10$, $Re_{imp} = 1000$, $r_\nu = 10$ and $R_s = 1$. The upper row is for $\theta_w = 60^\circ$ and the lower is for $\theta_w = 120^\circ$. From left to right, the times (scaled by T_{imp}) are 0, 1, 2, 3, 4, and 5.

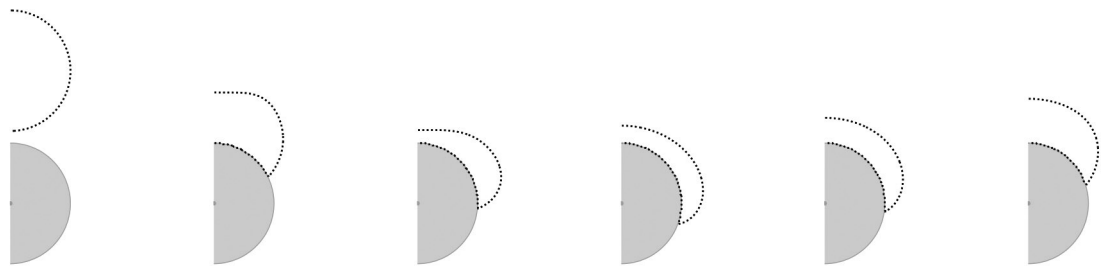

Fig. 22. Snapshots of a droplet impacting on a sphere at $We_{imp} = 10$, $Re_{imp} = 1000$, $r_\nu = 0.1$, $\theta_w = 60^\circ$ and $R_s = 1$. From left to right, the times (scaled by T_{imp}) are 0, 1, 2, 3, 4, and 5.

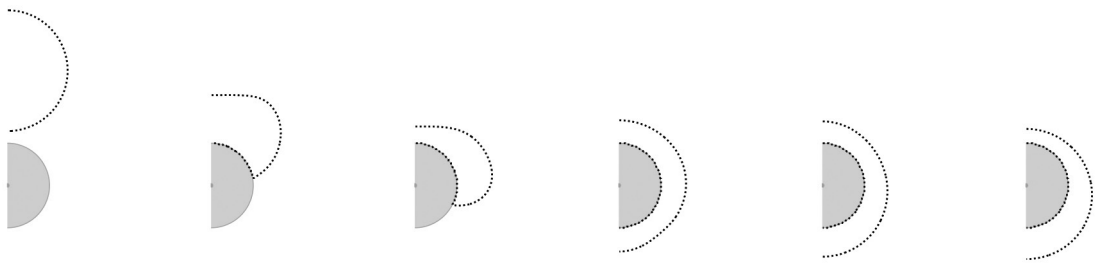

Fig. 23. Snapshots of a droplet impacting on a sphere at $We_{imp} = 10$, $Re_{imp} = 100$, $r_\nu = 10$, $\theta_w = 60^\circ$ and $R_s = 0.7$. From left to right, the times (scaled by T_{imp}) are 0, 1, 2, 4, 6, and 8.

0.7 with $Re_{imp} = 100$. Figure 22 plots the interfaces at selected times for the case with $r_\nu = 0.1$. In this case the ambient fluid is a hundred times more viscous than that for the above cases at $Re_{imp} = 1000$. By comparing fig. 22 and the first row of fig. 21, one can easily see the effect of the viscosity ratio. At $r_\nu = 0.1$, the droplet no longer breaks into a ring; instead, it simply deposits on the surface of the sphere after the initial deformation and retraction like what happens at $Re_{imp} = 100$ and $\theta_w = 60^\circ$. This is due to that the kinetic energy is quickly dissipated in the ambient fluid and the droplet loses its momentum too early to move further towards the other end. Figure 23 shows the evolution of the interface when the droplet impacts on a smaller sphere with $R_s = 0.7$ at $Re_{imp} = 100$. It is interesting to see that in this case the droplet covers the whole surface of the sphere after some time and then it

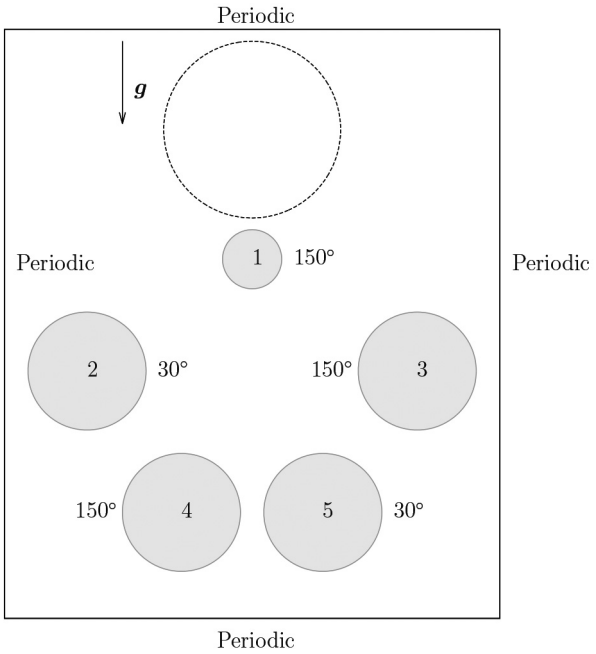

Fig. 24. Initial setup for a droplet impacting on five cylinders.

undergoes some oscillations while maintaining this special "completely engulfing" state. Although some researchers found that this state is less favorable energetically [34], the present simulation shows that the realization of this state (and even its maintenance) may not be that difficult. Of course, more work is required to find the specific conditions under which it can be initiated and preserved.

3.5 Droplet interaction with multiple objects

Finally, we do some study on a 2-D droplet impacting on several cylinders of different sizes and contact angles. The 2-D LBM was used. This problem is similar to the last case in [11]. The setup (and also the initial condition) of the problem is shown in fig. 24. Different from [11] we applied periodic boundaries (instead of wall boundaries) on the four sides of the domain. The radius of cylinder #1 is $R_{s1} = 0.25$, and all of the remaining four (cylinders #2-5) have a radius of 0.5 (*i.e.*, for this problem the reference length L_r is chosen to be the diameter of the large cylinders). The domain size is $L_x \times L_y = 4.2 \times 5$. The centers of the cylinders are fixed at $(x_{cs1}, y_{cs1}) = (2.1, 3.05)$, $(x_{cs2}, y_{cs2}) = (0.7, 2.1)$, $(x_{cs3}, y_{cs3}) = (3.5, 2.1)$, $(x_{cs4}, y_{cs4}) = (1.5, 0.9)$, and $(x_{cs5}, y_{cs5}) = (2.7, 0.9)$, and the contact angles on their outer surfaces are $\theta_{w1} = 150°$, $\theta_{w2} = 30°$, $\theta_{w3} = 150°$, $\theta_{w4} = 150°$, and $\theta_{w5} = 30°$, respectively. The radius of the drop is $R = 0.75$. Initially, its center is at $(x_{cd}, y_{cd}) = (2.1, 4.15)$ and its velocity is $(0, -U_{imp})$. A constant body force of magnitude g is applied downwards everywhere on the fluid. For this problem, there is an additional independent dimensionless parameters, the Froude number $Fr = U_{imp}^2/(gL_r)$. Here we set the density ratio as $r_\rho = 50$ (instead of $r_\rho = 1000$ in [11] due to the limitation of the 2-D code) and the kinematic viscosity ratio as $r_\nu = 0.8$. These give a dynamic viscosity ratio $r_\eta = 40$. The impact Weber and Reynolds numbers are $We_{imp} = 5$ and $Re_{imp} = 447$. These three parameters (r_η, We_{imp} and Re_{imp}) are the same as those in [11]. The Froude number is $Fr = 4.5$, which is half of that in [11]. That is, we applied a larger body force to expedite the process. Other simulation parameters are $N_L = 60$, $N_t = 1200$, $Cn = 0.06$, and $Pe = 5000$. The interface thickness W/δ_x is 3.6 lattice nodes. The radius of the sphere R_s is resolved by 15 nodes minimally (for $R_s = 0.25$) and 30 nodes maximally (for $R_s = 0.5$). Figure 25 shows six snapshots for this problem, which are similar to those reported in [11] to a large extent. First, the droplet is split into two parts by the small hydrophobic cylinder (#1). The generated satellite

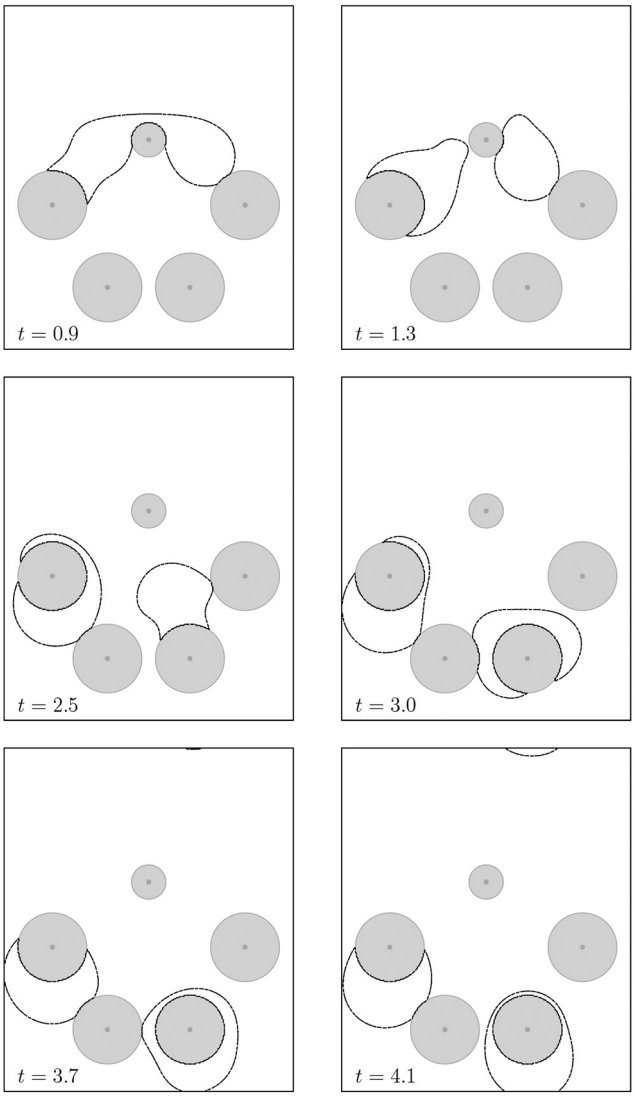

Fig. 25. Snapshots of a droplet impacting on five cylinders at $We_{imp} = 5$, $Re_{imp} = 447$, and $Fr = 4.5$. The density and viscosity ratios are $r_\rho = 50$, and $r_\nu = 0.8$ ($r_\eta = 40$). The times (scaled by T_{imp}) are 0.9, 1.3, 2.5, 3.0, 3.7, and 4.1.

droplet on the left side touches the hydrophilic cylinder (#2), spreads faster on it and leaves cylinder #1 earlier than the one on the right which contacts the hydrophobic cylinder (#3). The left satellite droplet then covers almost the whole outer surface of cylinder #2 and begins to touch cylinder #4 at the bottom under the action of body force. In contrast, the right droplet only passes cylinder #3 briefly and spreads on cylinder #5 which is hydrophilic. Finally, the left droplet is largely attached to the lower part of cylinder #4 whereas the right one engulfs cylinder #5 completely with a thin layer on its upper part. Because of the periodic boundary used here, a small portion of the right satellite droplet enters the domain from the top side in the later stage. In [11] finally both droplets spread on and stay in touch with the walls with a contact angle of 90°. By comparing the times of different events here and in [11], one finds that the increased body force indeed accelerates the penetration process.

4 Concluding remarks

To conclude, we have proposed and verified a new method for the wetting boundary condition on general surfaces immersed inside the domain for two-phase flow simulations. This method is relatively simple in the sense that only one point in the fluid domain is directly required to find the unknown value of the order parameter at a ghost point. At the same time, the accuracy is well maintained with the computational cost being only marginally higher. The application of this method for several problems demonstrated its capability to simulate complex problems with fluid interface and immersed solid objects with different wetting characteristics under 2-D, 3-D and cylindrical geometries. Preliminary studies of the droplet impact on a spherical particle indicate that totally different outcomes may appear depending on the impact Reynolds number, the viscosity ratio, the wettability as well as the size of the particle. Simulations of more complex flows including a droplet impacting on multiple objects have also been successfully performed. It should be noted that the proposed new implementation of the WBC is not restricted to hybrid lattice-Boltzmann finite-difference simulations. It can actually be used in other phase-field–based simulations of multiphase flows containing immersed solid walls as well. Finally, we also note that the present work has some limitations. The current axisymmetric LBM still cannot handle flows with density contrast. Substantial extensions must be made before it is applicable for such problems. Besides, the 2-D and 3-D LBM may encounter problems when the density ratio is too large. As the main focus is to treat immersed boundaries, we leave further development to overcome the limitations for future work.

This work is supported by the National Natural Science Foundation of China (NSFC, Grant No. 11202250). We thank the anonymous reviewers for very constructive comments.

Author contribution statement

J-JH had the idea for the new method and implemented it for 2-D, axisymmetric and 3-D models. All authors contributed to the simulations, data analysis and writing of the paper.

References

1. P.-G. de Gennes, F. Brochard-Wyart, D. Quere, *Capillarity and Wetting Phenomena: Drops, Bubbles, Pearls, Waves* (Springer, 2004).
2. Y. Sui, H. Ding, P.D.M. Spelt, Annu. Rev. Fluid Mech. **46**, 97 (2014).
3. R. Scardovelli, S. Zaleski, Annu. Rev. Fluid Mech. **31**, 567 (1999).
4. S. Osher, R. Fedkiw, *Level Sets Methods and Dynamic Implicit Surfaces* (Springer, 2002).
5. D.M. Anderson, G.B. McFadden, A.A. Wheeler, Annu. Rev. Fluid Mech. **30**, 139 (1998).
6. D. Jacqmin, J. Comput. Phys. **155**, 96 (1999).
7. V.E. Badalassi, H.D. Ceniceros, S. Banerjee, J. Comput. Phys. **190**, 371 (2003).
8. J.-J. Huang, H. Huang, X. Wang, Int. J. Numer. Methods Fluids **77**, 123 (2015).
9. H. Ding, P.D.M. Spelt, Phys. Rev. E **75**, 046708 (2007).
10. H.G. Lee, J. Kim, Comput. Fluids **44**, 178 (2011).
11. H.-R. Liu, H. Ding, J. Comput. Phys. **294**, 484 (2015).
12. A. Fakhari, D. Bolster, J. Comput. Phys. **334**, 620 (2017).
13. Y. Ge, L.-S. Fan, J. Fluid Mech. **573**, 311 (2007).
14. Y.-P. Li, H.-R. Wang, Can. J. Chem. Eng. **89**, 83 (2011).
15. D. Zhang, K. Papadikis, S. Gu, Int. J. Therm. Sci. **84**, 75 (2014).
16. Y. Liu, M. Andrew, J. Li, J.M. Yeomans, Z. Wang, Nat. Commun. **6**, 10034 (2015).
17. J.-J. Huang, H. Huang, C. Shu, Y.T. Chew, S.-L. Wang, J. Phys. A **46**, 055501 (2013).
18. T. Lee, Comput. Math. Appl. **58**, 987 (2009).
19. T. Lee, L. Liu, J. Comput. Phys. **229**, 8045 (2010).
20. J.J. Huang, C. Shu, Y.T. Chew, Int. J. Numer. Methods Fluids **60**, 203 (2009).
21. D. D'Humieres, I. Ginzburg, M. Krafczyk, P. Lallemand, L.-S. Luo, Philos. Trans. R. Soc. Lond. A **360**, 437 (2002).
22. P. Lallemand, L.-S. Luo, Phys. Rev. E **61**, 6546 (2000).
23. J. Kim, J. Comput. Phys. **204**, 784 (2005).
24. M. Bouzidi, M. Firdaouss, P. Lallemand, Phys. Fluids **13**, 3452 (2001).
25. Y. Peng, L.-S. Luo, Prog. Comput. Fluid Dyn. **8**, 156 (2008).
26. P. Yue, C. Zhou, J.J. Feng, J. Fluid Mech. **645**, 279 (2010).
27. E.W. Weisstein, *Spherical Cap*, `http://mathworld.wolfram.com/SphericalCap.html`.
28. P. Yue, C. Zhou, J.J. Feng, J. Comput. Phys. **223**, 1 (2007).
29. C. Pooley, H. Kusumaatmaja, J. Yeomans, Eur. Phys. J. ST **171**, 63 (2009).
30. S. Chibbaro, L. Biferale, F. Diotallevi, S. Succi, Eur. Phys. J. ST **171**, 223 (2009).
31. E.W. Washburn, Phys. Rev. **17**, 273 (1921).
32. J.-J. Huang, H. Huang, X. Wang, Phys. Fluids **26**, 062101 (2014).
33. A.L. Yarin, Annu. Rev. Fluid Mech. **38**, 159 (2006).
34. H.B. Eral, G. Manukyan, J.M. Oh, Langmuir **27**, 5340 (2011).